

A divergent astrocytic response to stress alters activity patterns via distinct mechanisms in male and female mice

Received: 24 September 2024

Accepted: 23 June 2025

Published online: 10 July 2025

Lewis R. Depaauw-Holt  ^{1,2}, Manon Duquenne  ^{1,2}, Sarah Hamane ², Sarah Peyrard ², Benjamin Rogers ^{1,2}, Clara Ireland ^{1,2}, Yusuke Nasu ^{3,4}, Stephanie Fulton ^{2,5}, Anthony Bosson  ², Thierry Alquier  ^{2,6} & Ciaran Murphy-Royal  ^{1,2} 

 Check for updates

The lateral hypothalamus is a brain region that regulates activity levels, circadian, and motivated behaviour. While disruption of these behaviours forms a hallmark of stress-related neuropsychiatric disorders, the underlying cellular mechanisms of how stress affects this brain region remain poorly understood. Here, we report that the effects of stress on behavioural activity levels correlate with spontaneous firing of orexin neurons, inducing hyperactivity in males and hypoactivity in female mice. These neuronal changes are accompanied by astrocyte remodelling, with causal manipulations identifying lateral hypothalamic astrocytes as key regulators of neuronal firing and physical activity patterns. In the context of stress, sex-specific changes in orexin neuron firing were driven by distinct astrocytic mechanisms with elevated purinergic signaling in male mice and reduced extracellular L-lactate in female mice. Finally, we show that genetic deletion of glucocorticoid receptors in lateral hypothalamic astrocytes restores key aspects of astrocyte morphology, rescues the effects of stress on orexin neuron firing, and recovers activity levels in both males and females. Overall, these data causally implicate astrocytes in the regulation of orexin neuron firing, behavioural activity patterns, and reveal that astrocytes are primary drivers of stress-induced behavioural change.

Astrocytes regulate multiple primary functions of the CNS¹ and have coalesced with neurons to form an important element of the tripartite synapse². Astrocytic contacts with distinct brain cell types are complex and dynamic³ enabling coordination of and active participation in a vast array of brain functions including synaptic transmission and plasticity^{4,5}, central metabolism⁶, and homoeostasis among other processes^{7,8}. Across experimental models, astrocytes display a high level of heterogeneity throughout the developing and ageing brain^{9,10}.

During post-natal development, astrocytes have been implicated in regulating the duration of “critical periods” by fine-tuning excitability of underlying neuronal circuits¹¹ and themselves display morphological and transcriptional phenotypes that coincide with important developmental milestones^{12,13}. Morphological alterations in astrocyte processes stand as a defining corollary in pathological brain states^{14–16}, with hallmark astrocytic responses to insult, stressors, and disease including changes in cell volume, evidenced by cellular atrophy or

¹Département de Neurosciences, Faculté de Médecine, Université de Montréal, Montréal, QC, Canada. ²Centre de Recherche du Centre, Hospitalier de l’Université de Montréal (CRCHUM), Montréal, QC, Canada. ³Institute of Biological Chemistry, Academia Sinica, Nankang, Taipei 115, Taiwan. ⁴Institute of Biochemical Sciences, National Taiwan University, Da'an, Taipei 106, Taiwan. ⁵Département de Nutrition, Faculté de Médecine, Université de Montréal, Montréal, QC, Canada. ⁶Département de Médecine, Faculté de Médecine, Université de Montréal, Montréal, QC, Canada.

 e-mail: ciaran.murphy-royal@umontreal.ca

hypertrophy depending on the pathological state^{17–23}. These volumetric aberrations are commonly associated with more discrete changes at the level of the peri-synaptic astrocyte process that is critical for regulating neurotransmitter^{24–27} and ionic homeostasis^{28–33} thereby modulating synaptic strength^{34–37}. Not surprisingly, alterations in astrocytic morphology have been shown to influence behaviours including learning and memory³⁸ and compulsive behaviours³⁹.

In the context of stress, astrocyte dysfunction has been shown to drive impairments in synaptic transmission and plasticity¹⁷, with long-lasting effects on learning and memory⁴⁰. In the cortex and hippocampus, stress blunts synaptic plasticity by uncoupling the astrocytic metabolic network, creating an energetic substrate deficit in neighbouring neuronal compartments¹⁷. Stress, however, results in swath of behavioural phenotypes including changes in sleep-wake^{41,42}, vigilance states^{43,44} and activity patterns⁴⁵, as well as motivated behaviours^{46,47}. One key brain hub that coordinates many of these behavioural processes is the lateral hypothalamus (LH), containing orexin (hypocretin) neurons^{48–51}. Orexin neuron firing is tightly controlled by multimodal mechanisms^{52–54} including local tuning by astrocytes^{55,56}. There is a strong body of work supporting a role for the astrocyte neuron lactate shuttle (ANLS) in fuelling orexin neuron firing with genetic perturbations of astrocyte function resulting in an instability of wakefulness^{52,55,56}, reminiscent of the effects observed following stress¹⁷. This led us to question whether astrocyte dysfunction in the LH directly contributes to stress-induced behavioural changes across the light-dark cycle.

Here, we investigated the effect of an early-life stressor on lateral hypothalamic astrocytes and their control of brain region dependent behaviour. We found that early-life stress induced long-term changes in blood glucocorticoid levels and altered activity levels in a sex-specific manner with reduced activity in female and increased activity in male mice. These endocrine and behavioural changes were associated with extensive remodelling of astrocyte morphology and distinct effects on orexin neuron firing patterns between sexes. We used chemogenetic manipulations to demonstrate that driving astrocyte activity was sufficient to induce increased activity levels and altered orexin neuron firing across both sexes. The mechanisms underlying stress-induced changes in orexin neuron firing were distinct between male and female mice, with elevated purinergic signalling in male mice driving hyperactivity and deficits in L-lactate availability in female mice decreasing neuronal firing and activity levels. Finally, we targeted glucocorticoid signalling specifically in LH astrocytes to assess whether stress signalling in these cells was necessary for cellular and behavioural phenotypes. LH astrocyte-specific deletion of glucocorticoid receptors following stress reversed the cellular and behavioural effects of early-life stress in both male and female mice. In conclusion, we reveal astrocytes as primary drivers of early-life pathological stress on neural activity and behaviour.

Results

Early Life Stress (ELS) elevates nadir blood glucocorticoids and perturbs diurnal activity rhythms

We leveraged a rodent model of ELS, including maternal separation (4h/day) between postnatal days (P)10-17 in combination with reduced bedding and nesting materials in all cages^{57,58} (Fig. 1A, B). As our previous work demonstrated this model of ELS induces a latent increase in blood glucocorticoids at P45⁴⁰, we set out to further examine whether this hormonal response was a consequence of a modified circadian set point. Consistent with previous data, we observed a rise in blood corticosterone in ELS mice at ZT2 (nadir/low) but not at ZT14 (zenith/high) (Fig. 1C). This increase was present in both male and female mice (Supplementary Fig. 1A). This elevation in blood corticosterone was accompanied by an increase in adrenal weight (Fig. 1D), which was driven primarily by female mice (Supplementary Fig. 1B). Like many other hormonal messengers, glucocorticoids are tightly regulated

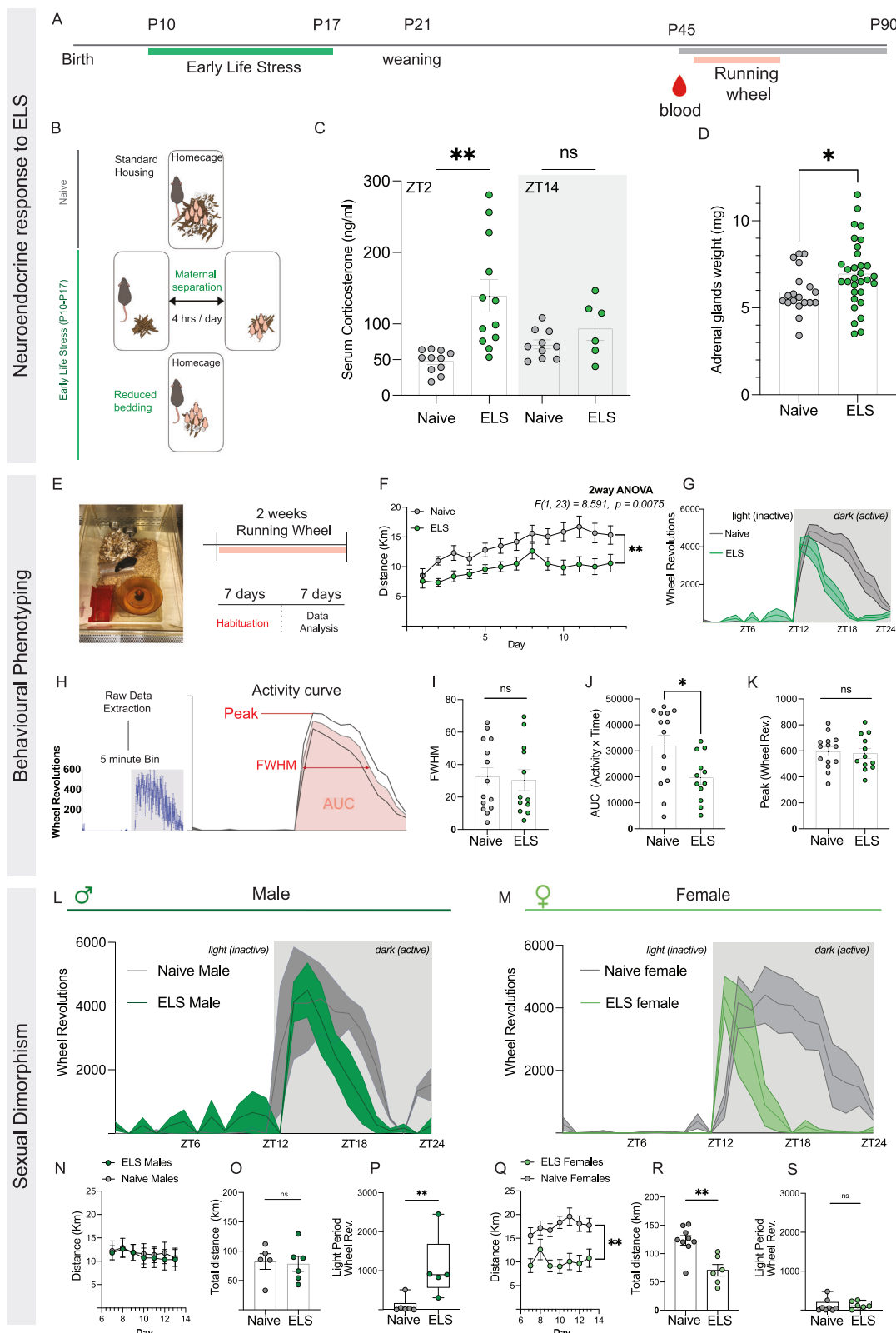
across the light-dark cycle^{59,60}, with chronically high levels associated with altered metabolism⁶¹, immune dysfunction⁶², and sleep-wake perturbation^{63,64}. Interestingly, both chronic stress, or chronic delivery of exogenous corticosterone, in rodents disrupts sleep patterns⁶⁵ and home cage running wheel activity^{66,67}, a behaviour strongly regulated in a circadian and diurnal manner. To test whether this ELS-induced hormonal response was associated with changes in activity levels we single-housed mice from naïve and ELS litters into cages with *ad libitum* access to a running wheel for two weeks (1 week of habituation followed by 1 week data collection) (Fig. 1E). Using both sexes, we observed a reduction in running wheel activity in ELS mice as measured by distance ran per day (Fig. 1F). This effect was due to an altered activity rhythm (Fig. 1G), where ELS mice exhibited hyperactivity during the light period (ZT0-12) and hypoactivity during the dark period (ZT12-24) resulting in diminished AUCs independent of peak running wheel activity (Fig. 1H–K). We next partitioned the data, separating males and females as stress can reveal strong sex differences^{68–70}, and found a striking difference in the effect of ELS on running wheel activity (Fig. 1L–S). Male mice subjected to ELS displayed no change in the distance ran per day but exhibited enhanced light period hyperactivity compared to naïve males (Fig. 1N–P, Supplementary Fig. 2A). The inverse was true for female ELS mice, with a reduction in the distance ran per day and no change in light period activity, exhibiting a behavioural phenotype isolated to the wake period (Fig. 1Q–S, Supplementary Fig. 2B). Further interrogation with a COSINOR analysis revealed no change in ELS male mice but a reduction in the MESOR of female ELS mice running wheel rhythms (Supplementary Fig. 2C, D). To determine whether the observed effects of ELS on running wheel activity were due to alterations in SCN-driven circadian rhythms, we conducted the same experiment in constant darkness. We observed no change in the distance ran per day or total distance in constant darkness in neither male (Supplementary Fig. 3A, B), nor female mice (Supplementary Fig. 3C, D), suggesting the effects of ELS on our running wheel phenotypes depend primarily on the presence of light cues rather than SCN generated rhythms alone.

This ELS paradigm has been shown to influence transcriptional profiles in reward centres of the brain^{57,71,72} suggesting our running wheel phenotype could be biased by a weakened hedonic drive in ELS mice. To answer this question, we subjected a cohort of ELS and naïve mice to a sucrose preference test (SPT) but saw no influence of stress on sucrose preference in either sex, ruling out anhedonia as a confounding factor (Supplementary Fig. 4).

To ascertain whether changes in running wheel activity were associated with basal metabolism and body composition, we first measured body weight of naïve and ELS mice across adolescence and into adulthood (P45–P150). Consistent with previous research^{73,74} we observed a reduction in body weight in both male and female ELS mice over time (Supplementary Fig. 5A, Supplementary Fig. 6A). We used echoMRI to assess whole body composition in live naïve and ELS mice and observed no change in lean mass and decreased fat mass in ELS male mice compared to controls (Supplementary Fig. 5B, C). Metabolic phenotyping revealed increased energy expenditure (normalised to lean mass) and activity (IR beam breaks in metabolic cage) in ELS male mice with no change in respiratory exchange ratios (RER) or food intake (Supplementary Fig. 5D–G). This increased energy expenditure and activity phenotype in metabolic cages is consistent with the hyperactivity profile observed using running wheels in home cages. In female mice, we observed no change in lean mass and fat mass (Supplementary Fig. 6B, C) with no alterations in energy expenditure, RER, or food intake (Supplementary Fig. 6D–G).

ELS modifies intrinsic firing properties of orexin neurons in a sexually dimorphic manner

We observed a clear sex difference in the behavioural response to ELS (Fig. 1), with male light period hyperactivity and female dark period



hypoactivity. Running wheel activity is entrained by multiple nuclei from a variety of brain regions⁷⁵⁻⁷⁷ including the lateral hypothalamus (LH)^{78,79}. The LH is a hub that integrates circadian inputs⁸⁰, metabolic cues⁸¹⁻⁸³, and local synaptic inputs^{84,85} to drive behavioural activity. Orexin neurons of the LH are wake promoting, and as such display higher activity during the onset of the dark period and are less active during the light period to allow for sleep onset and maintenance,

respectively⁵⁶. Recent work also demonstrated orexin neuron activity is time-locked to rodent running wheel use in a paradigm of temptation-resistant voluntary exercise⁷⁸. We next examined whether our observed changes in running wheel behaviour were associated with modifications in orexin neuron excitability.

To identify orexin neurons, we injected an AAV2/8-miniHCRT-tdTomato virus into the LH of naïve and ELS mice. After a minimum of

Fig. 1 | ELS induces elevations in blood corticosterone and differentially alters diurnal activity rhythms in male and female mice. **A** Experimental timeline with ELS occurring between P10-P17. **B** ELS paradigm; maternal separation 4 h/day and 70% reduced bedding in home cage and separation cages. **C** Serum corticosterone measurements significantly elevated at ZT2 (two-way ANOVA; $F(3,24) = 0.0020$. Tukey's multiple comparisons; Naïve ZT2 = 48.04 ng/ml, ± 4.76 ($N = 11$ mice), ELS ZT2 = 139.51 ng/ml, ± 22.5 ($N = 12$ mice), $p = 0.0011$. Naïve ZT14 = 71.21 ng/ml, ± 6.36 ($N = 10$ mice) vs ELS ZT14 = 93.75 ng/ml, ± 16.44 ($N = 6$ mice), $p = 0.876$). **D** Adrenal weight from Naïve and ELS mice (unpaired t test; Naïve = 5.91 mg, ± 0.287 ($N = 19$ mice), ELS = 6.95 mg, ± 0.349 ($N = 31$ mice), $p = 0.0427$). **E** Running wheel protocol; 2-week single housing with *ad libitum* access to horizontal running wheels. **F** Distance ran per day of Naïve ($N = 13$) and ELS ($N = 12$) mice (two-way ANOVA; $F(1,23) = 8.591$, $p = 0.0075$). **G** Representative 24-h trace of running wheel activity from Naïve and ELS mice. **H** Analyses of 24-hour running wheel activity curves from Naïve and ELS mice. **I** FWHM (Mann-Whitney test: Naïve = 32.44, ± 5.78 ($N = 14$), ELS = 30.41, ± 6.45 ($N = 12$), $p = 0.849$). **J** AUC (Mann-Whitney test: naïve = 31987, ± 3950 ($N = 14$), ELS = 19649, ± 2635 ($N = 12$), $p = 0.031$). **K** Peak wheel activity (unpaired t test: Naïve = 595.8 revolutions, ± 34.6 ($N = 14$), ELS revolutions = 580.6, ± 43.9 ($N = 12$), $p = 0.773$). **L** 24-h traces from Naïve and ELS male mice. **M** 24-h traces from Naïve and ELS female mice. **N** Distance ran per day (two-way ANOVA; $F(1,9) = 0.046$, $p = 0.834$) Naïve $N = 5$, ELS $N = 6$. **O** Total distance ran (Mann-Whitney test: Naïve = 82.40, ± 13.3 ($N = 5$), ELS = 78.42, ± 12.7 ($N = 6$), $p = 0.9307$), and (**P**) light-period activity counts (Mann-Whitney test: Naïve = 23.83, ± 82.1 ($N = 5$), ELS = 898.7, ± 360 ($N = 6$), $p = 0.0087$) for Naïve and ELS male mice. **Q** Distance ran per day (two-way ANOVA; $F(1,13) = 15.63$, $p = 0.0016$), Naïve $N = 9$, ELS $N = 6$. **R** Total distance ran (Unpaired t -test: Naïve = 123.3, ± 8.48 ($N = 9$), ELS = 70.64, ± 10.2 ($N = 6$), $p = 0.0016$), and (**S**) light-period activity counts (Mann-Whitney test: naïve = 50.17, ± 59.7 ($N = 9$), ELS = 108.8, ± 38.5 ($N = 6$), $p = 0.282$) for Naïve and ELS female mice. $N =$ mice. Bar charts = mean \pm S.E.M. Panels P and S = Median and I.Q.R = not significant, * $P < 0.05$, ** $P < 0.01$.

2 weeks, we prepared acute brain slices and performed whole-cell patch-clamp recordings of tdTomato+ cells in the peri-fornical area of the LH (Fig. 2A–C). We first validated the specificity of the AAV2/8-miniHCRT-tdTomato construct and found an average of 91.07% (± 4.49) of tdTomato+ cells colocalized with Orexin-A (Fig. 2B). Orexin neurons have unique electrophysiological signatures including low-threshold spikes after depolarising currents, inward rectification in response to hyperpolarising currents (I_h -current), and intrinsic firing rates of 2–4 Hz in the presence of 2.5 mM of glucose^{55,86,87}. We compared our tdTomato+ cells to biocytin filled orexin neurons, identified post-hoc through IHC, and report no significant differences in firing rates or resting membrane potentials (RMP) of these neurons, demonstrating no adverse effects of AAV2/8-miniHCRT-tdTomato expression on intrinsic membrane properties (Supplementary Fig. 7A). Of note, we also report a sex difference in naïve mice, where orexin neurons from female mice exhibit higher firing rates (5–7 Hz) compared to male mice (2–4 Hz) (Supplementary Fig. 7B), with no differences observed in other measures of intrinsic excitability such as input resistance (R_{in}) between male and female mice (Supplementary Fig. 7C, D). While there is a small body of literature demonstrating sex differences in orexin excitability with respect to mRNA expression (increased expression of c-fos)⁸⁸, this, to our knowledge, is the first demonstration of sex differences in basal orexin neurons firing.

We next conducted voltage-clamp recordings of orexin neurons to examine the effect of ELS on both spontaneous excitatory post-synaptic currents (sEPSC) and spontaneous inhibitory post-synaptic currents (sIPSC) (Fig. 2D–Q). To our surprise we observed no differences in sEPSC measures; frequency, peak amplitude, or inter-event interval (Fig. 2F–K). There was no change in sIPSC measures in male ELS mice (Fig. 2L–N) but we observed a reduction in the peak amplitude of sIPSC in female ELS mice (Fig. 2O). We then quantified the number of vesicular glutamate (VGluT) and vesicular GABA (VGaT) transporter puncta opposing orexin neurons to assess whether the functional changes were a consequence of altered structural pre-synaptic innervation (Supplementary Fig. 8A). We found no difference in VGaT+ puncta opposing orexin neurons in ELS male or ELS female mice (Supplementary Fig. 8A, B), but observed a decrease in VGluT apposition with orexin neurons in ELS female brains (Supplementary Fig. 8A, C). Further analysis investigating colocalization of synaptophysin (SP1) with postsynaptic density protein 95 (PSD-95) puncta to quantify active excitatory synapses in the LH, revealed no changes in synaptic density between ELS and naïve males or ELS and naïve females (Supplementary Fig. 8D, E), consistent with electrophysiological recordings.

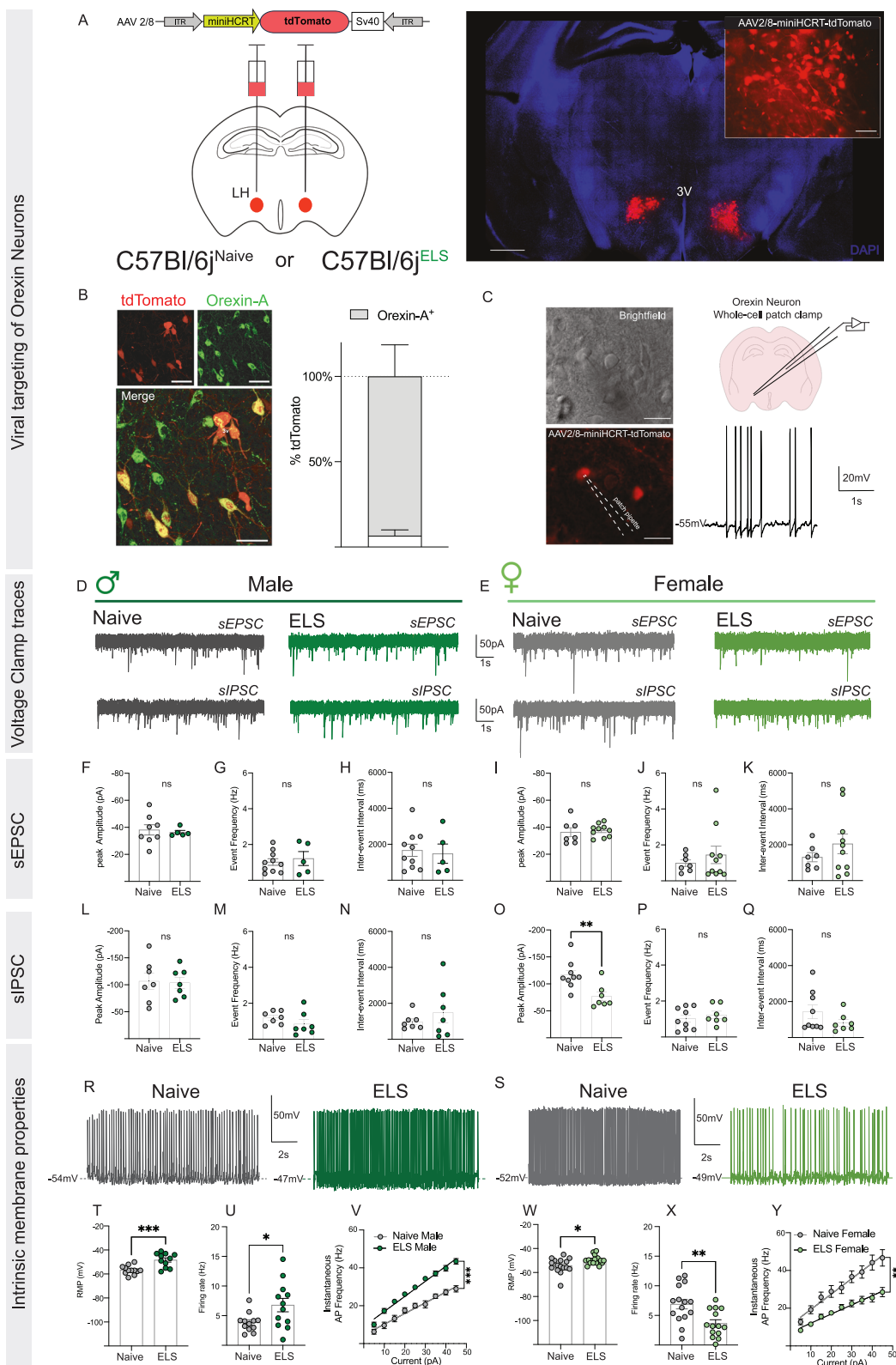
We then assessed intrinsic firing rates and observed a striking sex difference in response to ELS. Male ELS mice displayed elevated firing rates compared to naïve males (Fig. 2U), whereas firing rates were

greatly attenuated in female ELS mice (Fig. 2X). Additional analyses of intrinsic membrane properties of orexin neurons revealed a significant depolarisation of the RMP of orexin neurons from both male and female ELS mice (Fig. 2T, W). Furthermore, we observed larger increase in instantaneous firing rate in response to consecutively increasing 5 pA current injections in ELS male mice whereas the rate of firing was attenuated in ELS female mice after current injections (Fig. 2V, Y). Given the wake-promoting nature of orexin neurons, these results are consistent with our behavioural phenotypes, where male ELS mice displayed hyperactivity and elevated orexin neuron firing rates, and female ELS with hypoactivity and attenuated orexin neuron firing. These data demonstrate the sexually distinct effects of ELS on behaviour are reflected at the neuronal level in the LH.

ELS alters morphology of lateral hypothalamic astrocytes

Prior work has shown that astrocytic networks are required to meet metabolic demands and sustain orexin neuron firing to drive sleep-wake cycles^{55,56}. Considering our observed effects of ELS on orexin neuron excitability and the abundance of literature highlighting the acute and chronic effects of stress on astrocyte network and metabolic support capacity^{17,89–93}, we assessed the expression levels of two canonical markers for astrocytes comprising glial fibrillary acidic protein (GFAP); an intermediate filament protein and connexin-43 (Cx43); one of the functional gap-junction channel proteins in astrocytes that is critical for metabolic support of orexin neuron activity⁵⁵. We observed reductions in both GFAP and Cx43 in both male and female ELS mice (Fig. 3A–E) suggestive of cellular dysfunction. Additionally, this reduction in GFAP did not reflect a change in the number of GFAP+ cells (Supplementary Fig. 9A–C). These changes in structural proteins were not associated with changes in neuronal (Fig. 3F, G) nor astrocytic cell numbers (Fig. 3H).

Changes in GFAP expression have long been implicated in astrocytic “reactivity states” but GFAP expression levels are typically restricted to large primary branching processes which hinders accurate morphological characterisation¹⁹. To overcome this, we injected mice with a low-titre AAV2/5-GfaABC₁D-eGFP virus to sparsely label astrocytes⁹⁴ within the LH and conducted in-depth morphological analyses (Fig. 3I–R). Consistent with decreased GFAP expression levels, we observed a reduction in three-dimensional volume of LH astrocytes in both male and female ELS mice (Fig. 3K, O). Interestingly, we noted effects of ELS on process length and ramification in female mice (Fig. 3P, R), but not in male mice (Fig. 3L, N). We observed no differences in morphology of LH astrocytes in naïve male and female mice (Supplementary Fig. 9D–G). Taken together, our data reveal a reorganisation of astrocyte morphology in the LH of both male and female ELS mice in the absence of change to the number of neuronal and astrocytic cell types.



Driving astrocyte Gq-coupled calcium signalling in the LH impairs activity rhythms

Experimental manipulation of orexin neuron activity has been shown to directly influence wakefulness^{95,96} and wheel running behaviours⁷⁸. While ELS exerts profound effects on both diurnal activity rhythms and astrocytic morphology in the LH, it is unclear whether astrocytes directly participate in the regulation of running wheel activity across the

light-dark cycle. To address this, we used a chemogenetic approach to selectively drive astrocyte calcium activity in a temporally precise and brain-region specific manner. Compartmentalised fluctuations in astrocyte calcium have been shown to be a primary signalling mechanism by which astrocytes fine-tune neuronal output and behaviour^{39,97-101}. A cohort of naïve mice (male and female) were injected with hM3Dq- or hM4Di-coupled Designer Receptors Exclusively

Fig. 2 | ELS modifies intrinsic firing rates of orexin neurons in a sex specific manner. **A** Representative viral targeting of orexin neurons in the LH, scale bar = 1 mm & 25 μ m. **B** Validation of AAV2/8-miniHCRT-tdTomato construct, scale bar = 50 μ m. **C** Representative neurons from acute slice preparation under brightfield and Cy3 filter cube fluorescence with representative spontaneous firing rates of 3–4 Hz. **D, E** Representative traces of spontaneous excitatory post-synaptic currents (sEPSC) and spontaneous inhibitory post-synaptic currents (sIPSCs) from orexin neurons in voltage-clamp (-70 mV) configuration from Naïve and ELS mice. Male mice orexin neuron. **F** sEPSC peak amplitude (unpaired *t* test: Naïve = -38.14 pA, ± 3.81 ($N = 3, n = 8$ cells), ELS = -36.35 pA, ± 1.39 ($N = 2, n = 5$ cells), $p = 0.728$). **G** Event frequency (unpaired *t* test: Naïve = 1.022 Hz, ± 1.44 ($N = 3, n = 10$ cells), ELS = 1.215 Hz, ± 2.30 ($N = 2, n = 5$ cells), $p = 0.616$). **H** Inter-event interval (unpaired *t* test: Naïve = 1665 ms, ± 340 ($N = 3, n = 10$ cells), ELS = 1478 ms, ± 537 ($N = 2, n = 5$ cells), $p = 0.765$). **I** Female mice orexin neuron sEPSC peak amplitude (unpaired *t* test: Naïve = -37.57 pA, ± 3.32 ($N = 3, n = 7$ cells), ELS = -36.31 pA, ± 1.50 ($N = 3, n = 10$ cells), $p = 0.705$). **J** Event frequency (Mann–Whitney test: Naïve = 0.836 Hz, ± 0.183 ($N = 3, n = 7$ cells), ELS = 0.853 Hz, ± 0.485 ($N = 3, n = 10$ cells), $p = 0.720$). **K** Inter-event interval (unpaired *t* test: Naïve = 1306 ms, ± 257 ($N = 3, n = 7$ cells), ELS = 2049 ms, ± 550 ($N = 3, n = 10$ cells), $p = 0.303$). Male mice orexin neuron. **L** sIPSC peak amplitude (unpaired *t* test: Naïve = -106.8 pA, ± 15.1 ($N = 2, n = 7$ cells), ELS = -103.8 pA, ± 10.1 ($N = 2, n = 7$ cells), $p = 0.871$). **M** Event frequency (unpaired *t* test: Naïve = 1.022 Hz, ± 0.135 ($N = 2, n = 7$ cells), ELS = 1.215 Hz, ± 0.246 ($N = 2, n = 8$ cells), $p = 0.230$). **N** Inter-event interval (unpaired *t* test: Naïve = 980.1 ms, ± 169 ($N = 2, n = 7$ cells), ELS = 1489 ms, ± 555 ($N = 2, n = 7$ cells), $p = 0.398$). Female mice orexin neuron. **O** sIPSC peak amplitude (unpaired *t* test: Naïve = -116.5 pA, ± 8.77 ($N = 2, n = 9$ cells),

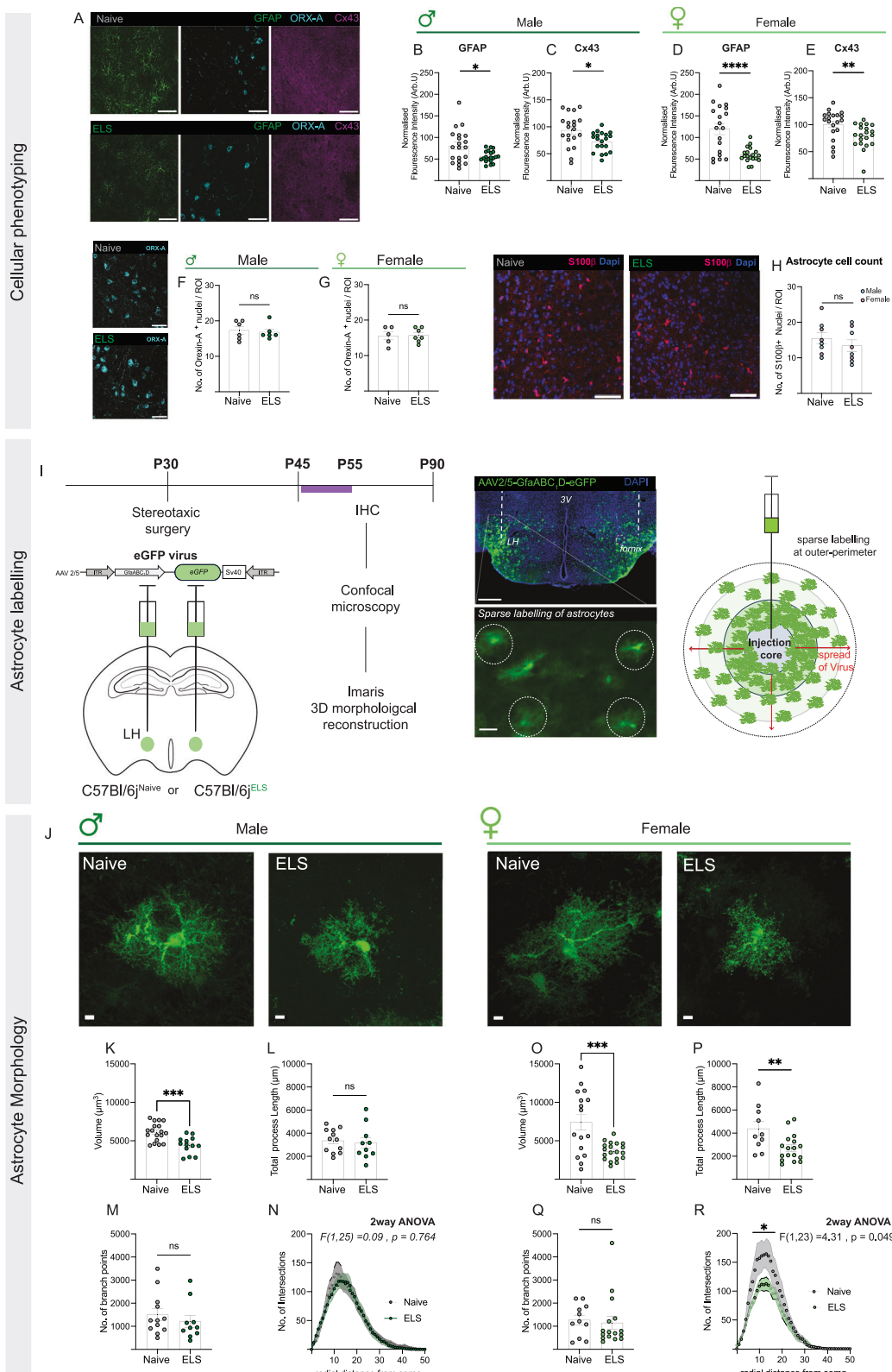
ELS = -76.9 pA, ± 8.34 ($N = 2, n = 9$ cells), $p = 0.0064$). **P** Event frequency (unpaired *t* test: Naïve = 1.012 Hz, ± 0.203 ($N = 2, n = 7$ cells), ELS = 1.230 Hz, ± 0.203 ($N = 2, n = 9$ cells), $p = 0.468$). **Q** Inter-event interval (Mann–Whitney test: Naïve = 1431 ms, ± 373 ($N = 2, n = 7$ cells), ELS = 824.5 ms, ± 194 ($N = 2, n = 9$ cells), $p = 0.252$). **R** Representative traces of spontaneous firing rates of orexin neurons from Naïve and ELS male mice. **S** Representative traces of spontaneous firing rates of orexin neurons from Naïve and ELS female mice. **T** Resting membrane potentials (RMP) of orexin neurons from Naïve and ELS male mice (unpaired *t* test: Naïve = -56.65 mV, ± 1.04 ($N = 3, n = 12$ cells), ELS = -48.36 mV, ± 1.78 ($N = 4, n = 11$ cells), $p = 0.0005$). **U** Spontaneous firing rates of orexin neurons from Naïve and ELS male mice (unpaired *t* test: Naïve = 3.85 Hz, ± 0.459 ($N = 4, n = 12$ cells), ELS = 6.789 Hz, ± 1.13 ($N = 4, n = 12$ cells), $p = 0.025$). **V** Instantaneous AP frequency of orexin neurons from Naïve ($N = 5, n = 14$) and ELS ($N = 5, n = 11$) male mice in response to 5 pA incremental current injections (two-way repeated measures ANOVA; $F(1,23) = 40.60, p = < 0.001$). Naïve $N = 4, n = 14$ cells, ELS $N = 4, n = 11$ cells. **W** Resting membrane potentials (RMP) of orexin neurons from Naïve and ELS female mice (unpaired *t* test: Naïve = -54.19 mV, ± 1.53 ($N = 4, n = 16$ cells), ELS = -49.66 mV, ± 0.930 ($N = 4, n = 16$ cells), $p = 0.0169$). **X** Spontaneous firing rates of orexin neurons from Naïve and ELS female mice (unpaired *t* test: Naïve = 6.91 Hz, ± 0.807 ($N = 4, n = 15$ cells), ELS = 3.648 Hz, ± 0.618 ($N = 4, n = 14$ cells), $p = 0.0037$). **Y** Instantaneous AP frequency of orexin neurons from Naïve ($N = 3, n = 9$) and ELS ($N = 3, n = 10$) female mice in response to 5 pA incremental current injections (two-way repeated measures ANOVA; $F(1,17) = 15.67, p = < 0.01$). N = mice, n = cells. Bar charts = mean \pm S.E.M. ns = not significant, $*P < 0.05$, $**P < 0.01$.

Activated by Designer Drugs (DREADDs) under the control of GfaABC₁D promoter to selectively induce calcium fluctuations in LH astrocytes, as both hM3Dq and hM4Di have been shown to increase calcium^{97,102} (Fig. 4A, Supplementary Fig. 10). To chemogenetically activate astrocytes, Clozapine-N-Oxide (CNO) was added to the drinking water for 3 days at 1.25 mg/kg standardised to water intake and body weight (Fig. 4B, C). Oral delivery of CNO was chosen to mitigate stress associated with repeated intraperitoneal injection. Remarkably, we report an effect of CNO-induced astrocyte activation on running wheel behaviour exclusively in hM3Dq-injected mice (Fig. 4D–G) and not in hM4Di-injected or mCherry-injected controls (Supplementary Fig. 10). hM3Dq-injected mice exhibited elevations in light period wheel activity and reduced dark period wheel activity after administration of CNO (Fig. 4F, G). This isolated effect of hM3Dq- and not hM4Di- activation was consistent at 3 ascending doses of CNO (Supplementary Fig. 11). To assess the effects of driving hM3Dq coupled calcium on LH astrocyte morphology we injected a separate cohort of mice with AAV2/5-GfaABC₁D-hM3Dq and a low titre AAV2/5-GfaABC₁D-eGFP virus to sparsely label astrocytes (Fig. 4H–P), before delivery of CNO in the drinking water for 3 days, sacrificing mice at lights-off (ZT0; 72 hours total of CNO exposure), and conducted 3D morphological analyses. Curiously, driving hM3Dq in male mice had negligible effects on LH astrocyte morphology (Fig. 4I–L) however, we saw a reduction in total process length and the number of branch points in female mice (Fig. 4M–O). There was a reduction in branching intersections in female hM3Dq injected mice, which mirrored the morphological modifications induced by ELS (Fig. 4P). We assessed the levels of Cx43 after driving hM3Dq in astrocytes, though saw no effect in either sex (Supplementary Fig. 12). We next examined the consequences of driving hM3Dq signalling in astrocytes on the firing rates of nearby orexin neurons (Fig. 4Q–U). We injected naïve mice with AAV2/5-GfaABC₁D-hM3Dq and AAV2/8-miniHCRT-tdTomato viruses and prepared acute brain slices of the LH. We conducted whole-cell patch clamp recording of orexin neurons and bath applied CNO (10 μ M) for 3 min to selectively activate hM3Dq signalling in LH astrocytes. Bath application of CNO increased the firing rate in both male and female mice injected with hM3Dq (Fig. 4S, T). Taken together, these experiments suggest that driving astrocyte calcium activity is sufficient to elevate orexin neuron firing and drive running wheel activity.

ELS elevates purinergic signalling in orexin neurons in male mice

Manipulation of astrocytic Gq-signalling recapitulated the elevated firing rates observed in ELS male mice. There is an abundance of literature demonstrating the modulatory effects of astrocyte-derived purines on local synaptic activity^{103–107} with the release of ATP from astrocytes a direct consequence of intracellular Gq-coupled signalling pathway activation¹⁰⁶. While in the hippocampus, ATP released from astrocytes is rapidly converted to adenosine that acts pre-synaptically to inhibit synaptic transmission¹⁰⁸, in the hypothalamus ATP can act on post-synaptic receptors to bolster neuronal transmission^{107,109}. As we observed no dramatic changes in sEPSC or sIPSC, we reasoned the mechanism driving male orexin neuron firing could have a post-synaptic locus. We prepared acute brain slices from ELS and naïve male mice to perform whole-cell patch clamp recordings of orexin neurons combined with pharmacological manipulation of purinergic signalling (Fig. 5A, B). To assess the contribution of adenosine signalling in our phenotype in ELS male mice we bath applied 200 nM of selective adenosine A1 receptor antagonist 8-cyclopentyltheophylline (CPT) (Fig. 5C–E). We observed a modest but significant reduction in firing of orexin neurons from naïve male mice in response to CPT, but no effect in ELS male mice (Fig. 5D, E). Furthermore, we saw no effect on firing rate after bath application of adenosine A2 receptor antagonist ZM 241385 in neither naïve nor ELS mice (Fig. 5F–H). These data highlight the modest influence of adenosine signalling on orexin neuron activity in naïve mice. Interestingly, the complete absence of the effect of CPT in ELS mice suggests a lack of adenosine tone, which could contribute to heightened wakefulness.

Next, we set out to evaluate whether increased firing in male mice following ELS could result from increased ATP acting on purinergic receptors. We next bath applied 10 μ M of PSB12379, a selective inhibitor of CD73, the ecto-5'-nucleotidase responsible for conversion of AMP to adenosine. Conceptually, bath application of PSB12379 should increase the relative amount of extracellular ATP by impairing its downstream conversion to adenosine (Fig. 5A). We observed a robust increase in the firing rate of orexin neurons in naïve mice (Fig. 5I, J), with a modest increase in firing observed in ELS mice (Fig. 5K), suggestive of tonically elevated extracellular ATP tone that could be responsible for increased firing of orexin



neurons in ELS male mice. Previous research indicates that orexin neurons express purinergic receptors including the P2X2 ionotropic ATP receptor¹¹⁰. Indeed, using the broad spectrum P2 receptor antagonist PPADS tetrasodium salt (50 μM), we observed an attenuation of the firing rate of orexin neurons in ELS male mice (Fig. 5L–N), without any impact in naïve mice (Fig. 5L–N). To isolate the contribution of P2X receptors, we next bath applied 50 μM of

iso-PPADS, a P2X receptor antagonist, and again saw a strong reduction in orexin neuron firing in ELS compared to naïve mice (Fig. 5O–R). To assess mechanistic specificity, we repeated this final experiment in female mice and showed that *iso*-PPADS failed to alter the firing rate of orexin neurons from ELS female mice (Supplementary Fig. 13), suggesting elevated P2X signalling is a male-specific consequence of ELS.

Fig. 3 | ELS modifies astrocyte morphology in the LH. **A** Representative IHC of GFAP, Orexin-A, and Cx43, in the LH of Naïve and ELS mice, scale bars = 25 μ m. **B, C** Normalised fluorescence intensity (Arb.U.) measures of GFAP and Cx43 in the LH of Naïve and ELS male mice. **B** GFAP - unpaired *t* test: Naïve = 80.33Arb.U., \pm 8.64 (N = 4, n = 20 cells), ELS = 55.91Arb.U., \pm 3.01 (N = 4, n = 20 cells), p = 0.011. **C** Cx43 - unpaired *t* test: Naïve = 93.74Arb.U., \pm 6.79 (N = 4, n = 20 cells), ELS = 72.68Arb.U., \pm 4.02 (N = 4, n = 20 cells), p = 0.011. **D, E** Normalised fluorescence intensity (Arb.U.) measures of GFAP and Cx43 in the LH of Naïve and ELS female mice. **D** GFAP - unpaired *t* test: Naïve = 119.2Arb.U., \pm 12.7 (N = 4, n = 19 cells), ELS = 58.87Arb.U., \pm 3.91 (N = 4, n = 19 cells), p < 0.0001. **E** Cx43 - unpaired *t* test: Naïve = 100.8Arb.U., \pm 6.02 (N = 4, n = 20 cells), ELS = 79.27Arb.U., \pm 4.98 (N = 4, n = 20 cells), p = 0.009. **F** Quantification of Orexin-A+ cells between Naïve and ELS male mice (unpaired *t* test: Naïve = 17.33 cells, \pm 1.09 (N = 6), ELS = 16.83 cells, \pm 0.872 (N = 6), p = 0.727) and **(G)** Naïve and ELS female mice (unpaired *t* test: Naïve = 15.60 cells, \pm 1.66 (N = 5), ELS = 15.71 cells, \pm 0.747 (N = 7), p = 0.933). **H** Quantification of S100 β + astrocytes in the lateral hypothalamus (unpaired *t* test: Naïve = 14.50 (N = 8), ELS = 12.00 (N = 8), p = 0.367) scale bars = 25 μ m. **I** Experimental timeline and viral constructs for sparse

labelling of astrocytes in the LH. Scale bars = 50 μ m. **J** Representative AAV-GfaABC1D-eGFP expressing astrocytes in the LH from Naïve and ELS mice, scale bars = 5 μ m. Morphological reconstruction of LH astrocytes from Naïve and ELS male mice. **K** Volume (unpaired *t* test: Naïve = 5916 μ m 3 , \pm 2.797 (N = 4, n = 18 cells), ELS = 4430 μ m 3 , \pm 308 (N = 3, n = 13 cells), p = 0.0004). **L** Total process length (unpaired *t* test: Naïve = 3365 μ m \pm 293 (N = 3, n = 12 cells), ELS = 3168 μ m, \pm 471 (N = 3, n = 10 cells), p = 0.717). **M** No. of branch points (Mann-Whitney test: Naïve = 1256 branch points \pm 264 (N = 3, n = 12 cells), ELS = 943 branch points, \pm 263 (N = 3, n = 10 cells) p = 0.314). **N** Sholl analysis (two-way ANOVA; F (1,25) = 0.09, p = 0.764). Morphological reconstruction of LH astrocytes from Naïve and ELS female mice. **O** Volume (unpaired *t* test: Naïve = 7740 μ m 3 , \pm 1041 (N = 4, n = 16 cells) ELS = 3659 μ m 3 , \pm 257 (N = 4, n = 19 cells), p = 0.0006). **P** Total process length (unpaired *t* test: Naïve = 4396 μ m, \pm 627 (N = 3, n = 10 cells), ELS = 2701 μ m, \pm 278 (N = 4, n = 17 cells), p = 0.009). **Q** No. of branch points (Mann-Whitney test: Naïve = 1209 branch points, \pm 211 (N = 3, n = 11 cells), ELS = 720.5 branch points, \pm 278 (N = 4, n = 16 cells) p = 0.488). **R** Sholl analysis (two-way ANOVA; F (1,23) = 4.31, p = 0.049). N = mice, n = cells. Bar charts = mean \pm S.E.M. ns = not significant, * P < 0.05, ** P < 0.01.

ELS impairs lactate availability in female mice

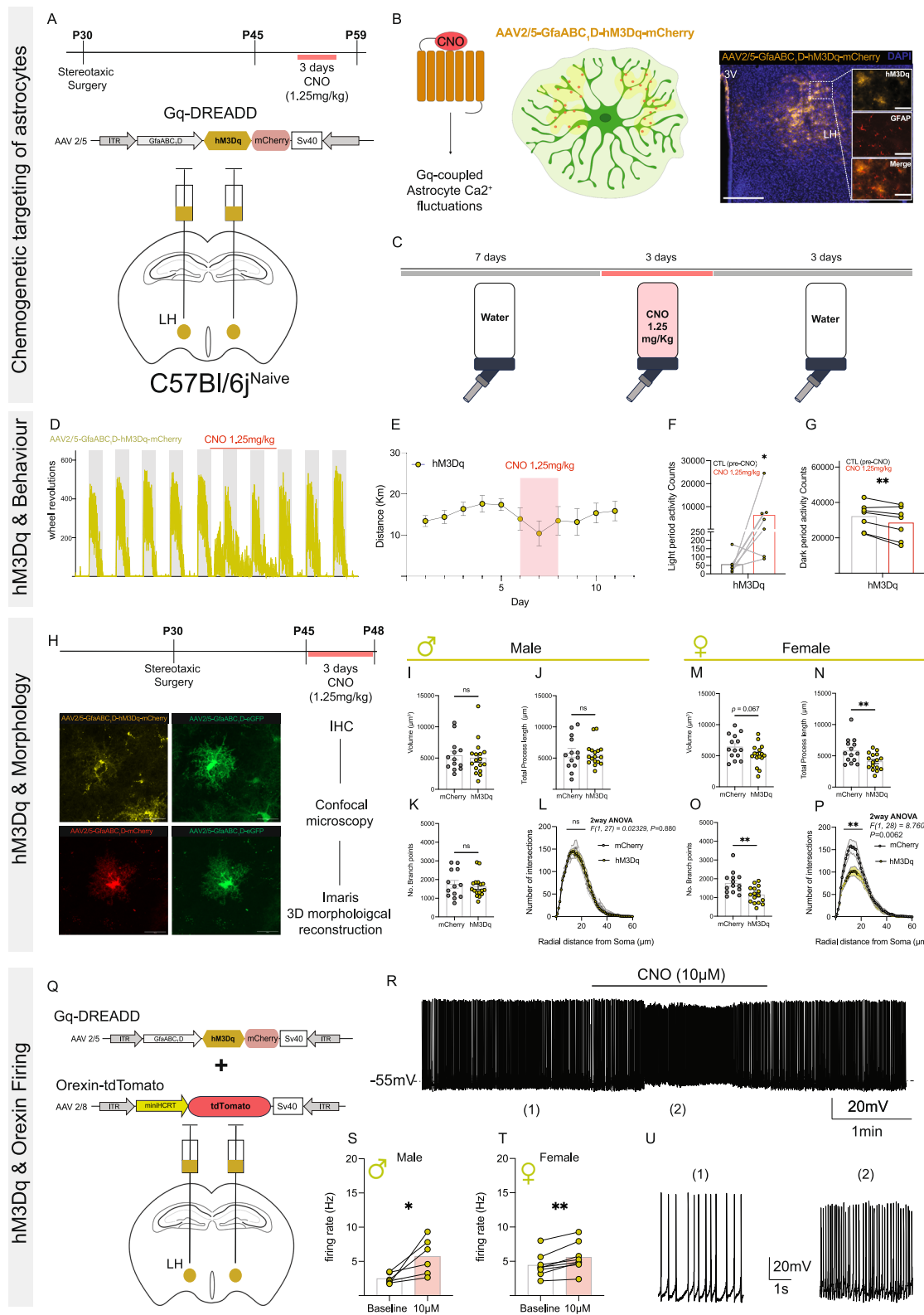
ELS reduced orexin neuron firing in female mice (Fig. 2K, M) that was associated with reduced expression of the astrocytic gap junction channel Cx43 (Fig. 3C), decreased astrocyte volume, and reduced process branching (Fig. 3J). As there is an extensive body of literature linking changes in Cx43 expression with synaptic energetics via L-lactate shuttling from astrocytes to neurons, we set out to test whether dysfunction in the astrocyte-to-neuron L-lactate shuttle (ANLS) was responsible for the electrophysiological phenotype observed following ELS in female mice. Indeed, bath application of 5 mM of L-lactate, while having no effect in naïve female male mice (Fig. 6A, E), restored firing rates in ELS female mice (Fig. 6C, F). This same manipulation in male mice had no effect in naïve nor ELS conditions (Fig. 6B, D, G, H), again supporting sex-specific changes on the sub-cellular level producing diverse endophenotypes.

To confirm these observations, we employed a novel genetically encoded fluorescent sensor for intracellular L-lactate iLACCO2.0, an improved variant of iLACCO1.0¹¹. We used a viral approach to express this sensor using a synapsin promotor to visualise intracellular L-lactate in LH neurons (AAV2/9-hSyn-iLACCO2.0) from naïve and ELS female mice (Fig. 6I). We prepared acute brain slices of the LH and conducted two-photon imaging of intracellular L-lactate dynamics within neurons during baseline, and responses to extracellular application of L-lactate (Fig. 6J, K). We hypothesised that if there is a L-lactate deficit in ELS female mice, we would expect a larger increase in fluorescence (df/f) in response to L-lactate application, whereas in naïve female mice fluorescence changes would be negligible as extracellular L-lactate levels are tightly regulated by the ANLS. Consistent with hypothesis, we observed a robust increase in fluorescence of the intracellular L-lactate sensor in response to 5 mM L-lactate in ELS female neurons but not naïve females (Fig. 6L, M). Taken together these data suggest that changes in astrocytic gap-junction channel expression are linked to impaired ANLS evidenced by reduced extracellular L-lactate availability in the LH and decreased orexin neuron firing in female mice subjected to ELS.

Astrocyte glucocorticoid receptor KO rescues the cellular & behavioural effects of ELS

So far, we have shown that ELS impacts endocrine function, activity levels, orexin neuron firing, and astrocyte morphology. This resulted in hyperexcitability and increased ATP signalling in male and hypoexcitability and decreased energy substrate availability in female mice. These divergent effects between sexes must share a common mechanism as both sexes undergo identical stress exposure. Prior work demonstrated that astrocytes are highly sensitive to glucocorticoids, with glucocorticoid signalling directly impeding gap-junction coupling in these cells

and supply of L-lactate to synapses¹⁷, reminiscent of our mechanistic observations in female mice. Independent work has also shown that spinal cord astrocytes when exposed to glucocorticoids can increase ATP release from these cells¹⁰⁷, again reminiscent of our mechanistic findings in male mice. These studies however, failed to consider both sexes and whether divergent astrocytic responses to stress may exist. To determine whether glucocorticoid signalling in astrocytes reflects a common target between sexes, we first conducted immunostaining against glucocorticoid receptors (GR) in the LH and found that ELS increased nuclear localisation of GRs in astrocytes, a proxy for GR activation⁴⁰ in both male and female mice (Supplementary Fig. 14A, B), suggestive of a shared mechanism. To test this, we used a combination of transgenic mouse lines and viral delivery of *cre-recombinase* to target GR signalling in a cell-type specific and brain region specific manner. The selective deletion of astrocytic GRs in the LH was achieved using a transgenic mouse line with a floxed Nuclear Receptor Subfamily 3 Group C Member 1 (*Nr3c1*^{fl/fl}) allele. *Nr3c1*^{fl/fl} mice were bilaterally injected with AAV2/5-GfaABC1D-Cre-eGFP to delete GRs in astrocytes exclusively in the LH [GR^{KO}] (Fig. 7A). Stereotaxic surgery was completed at P30 (13 days after ELS) allowing sufficient time for viral mediated deletion of GR prior to behavioural and synaptic experiments. Cre-injected mice were compared to both ELS *Nr3c1*^{fl/fl} and naïve *Nr3c1*^{fl/fl} mice injected with a control virus (AAV2/5-GfaABC1D-eGFP). We report that this approach did not influence neuronal (Orexin-A+) or astrocyte (S100 β +) cell counts (Fig. 7B, C), and cre-recombination was restricted to astrocytes with a cell specificity of 94.5% (\pm 4.41) in S100 β + astrocytes and expression efficiency of 89.3% (\pm 5.61) (Fig. 7D Supplementary Fig. 15D, E). We next stained AAV2/5-GfaABC1D-Cre-eGFP injected brain slices with an anti-cre antibody to ensure that *cre recombinase* expression was restricted to cells expressing the eGFP reporter gene (Supplementary Fig. 15F-H). We found 97.9% of eGFP+ cells expressed Cre and 100% of Cre cells were eGFP+, confirming no ectopic expression of Cre outside of the eGFP reporter (Supplementary Fig. 15G). While S100 β is a valuable marker for astrocytes, there have been reports of mild expression in NG2 glia¹¹² and oligodendrocyte progenitor cells¹¹³, therefore we further validated expression of eGFP-Cre+ with a distinct astrocyte marker glutamine synthetase (GS). Again, we report similar findings with 96.6% of eGFP-Cre+ cells were GS+ (Supplementary Fig. 16B). As Cre expression was constricted to eGFP+ cells only, we then assessed the number of NeuN+ cells that colocalised with eGFP-Cre. We found 0% of Cre-eGFP expressed in NeuN+ cell types (Supplementary Fig. 16C, D), further supporting high levels of specificity of this approach. Compared to control astrocytes (Cre-negative) within the same brain and eGFP-control astrocytes from injected littermates, we observed a reduction in nuclear GR fluorescence (Supplementary Fig. 15A-C), as expected.



Using this robust approach, we assessed the influence of astrocytic GR^{KO} on astrocyte morphology in the LH using the same low-titre viral targeting approach but found no effect of astrocytic GR^{KO} on total volume of astrocytes (Fig. 7G, J). We did however, observe a striking increase in the number of branch points/total volume, in both male and female ELS-GR^{KO} astrocytes (Fig. 7H, K). Next, we questioned whether GR^{KO}-induced morphological reorganisation influenced Cx43

expression, one hallmark of this ELS model⁴⁰. We observed an increase in Cx43 fluorescence in ELS-GR^{KO} astrocytes compared to control ELS-eGFP astrocytes in both male and female mice (Fig. 7I, L). To determine whether this manipulation also attenuated the downstream neuronal deficits (Fig. 2) we conducted further stereotaxic surgeries in a separate cohort of ELS-Nr3c1^{fl/fl} mice to enable dual expression of AAV2/5-GfaABC₁D-Cre-eGFP in LH astrocytes with AAV2/8-miniHCRT-

Fig. 4 | Gq-coupled calcium fluctuations in LH astrocytes excites orexin neurons to perturb diurnal activity rhythms in naïve mice. **A** Chemogenetic construct & timeline. **B, C** Expression in LH astrocytes and chronic delivery of clozapine-N-oxide (CNO) in drinking water (1.25 mg/kg). Scale bar = 100 μ m. **D** Representative traces of running wheel activity from hM3Dq-injected mice ($N = 7$). **E** Distance ran per day, ($N = 7$). **F** Quantification of light period activity pre and during delivery of CNO (ratio paired t test: $t_6 = 3.34, p = 0.016, N = 7$). **G** Quantification of dark period activity pre and during delivery of CNO (paired t test: $t_5 = 3.96, p = 0.0074, N = 7$). **H** Experimental timeline and representative AAV-GfaABC₁D-eGFP expressing astrocytes in the LH from hM3Dq- or mCherry mice, scale bars = 20 μ m. Morphological reconstruction of LH astrocytes from or mCherry and hM3Dq injected male mice: **I**) Volume (unpaired t test: mCherry = 5389 μ m³, \pm 708 ($N = 3, n = 13$ cells), hM3Dq = 5015 μ m³, \pm 670 ($N = 3, n = 15$ cells), $p = 0.707$), **J**) Total process length (unpaired t test: mCherry = 5813 μ m, \pm 257 ($N = 3, n = 13$ cells), hM3Dq = 5593 μ m, \pm 441 ($N = 3, n = 17$ cells), $p = 0.793$), **K**) No. of branch points (Mann-Whitney test: mCherry = 1632 branch points, \pm 207 ($N = 3, n = 13$ cells), hM3Dq = 1445 branch points, \pm 137 ($N = 3, n = 17$ cells) $p = 0.893$), **L**)

Sholl analysis (two-way ANOVA: $F(1,27) = 0.0233, p = 0.880$). Morphological reconstruction of LH astrocytes from or mCherry and hM3Dq injected female mice: **M**) Volume (unpaired t test: mCherry = 6418 μ m³, \pm 527 ($N = 3, n = 14$ cells), hM3Dq = 5132 μ m³, \pm 434 ($N = 3, n = 16$ cells), $p = 0.0678$), **N**) Total process length (unpaired t test: mCherry = 5798 μ m, \pm 534 ($N = 3, n = 14$ cells), hM3Dq = 4083 μ m, \pm 330 ($N = 3, n = 16$ cells), $p = 0.009$), **O**) No. of branch points (unpaired t test: mCherry = 1754 branch points \pm 156 ($N = 3, n = 13$ cells), hM3Dq = 1139 branch points, \pm 109 ($N = 3, n = 17$ cells) $p = 0.0027$), **P**) Sholl analysis (two-way ANOVA: $F(1,28) = 8.76, p = 0.0062$). **Q** Co-injection of hM3Dq and miniHCRT-tdTomato virus into the LH. **R** Representative trace of orexin neuron spontaneous AP firing in current clamp with 3 min bath application of CNO (10 μ M). **S** Change orexin neuron spontaneous firing rate in male mice ($N = 3, n = 6$ cells) after bath application of CNO (paired t test: $t_5 = 2.94, p = 0.032$). **T** Change orexin neuron spontaneous firing rate in female mice ($N = 3, n = 8$ cells) after bath application of CNO (paired t test: $t_7 = 4.94, p = 0.0017$). **U** Representative firing rate of orexin neuron firing rates at baseline (1) and with CNO (2). N = mice, n = cells. Bar charts = mean \pm S.E.M. ns = not significant, * $P < 0.05$, ** $P < 0.01$.

tdTomato to identify orexin neurons (Fig. 5M). Patch-clamp electrophysiology from genetically identified orexin neurons in astrocyte GR^{KO} mice revealed that not only did astrocytic GR^{KO} in the LH correct the ELS-induced changes in firing rate and RMP of orexin neurons, but it did so in a sex specific manner, attenuating the elevated firing rates in male ELS mice (Fig. 7N–P) and restoring reduced firing rates female ELS mice (Fig. 7Q–S). These data highlight astrocyte GR signalling as a convergent mechanism, responsible for the effects of ELS on cellular scales that is shared between the sexes.

In light of these results, we conducted stereotaxic surgeries to induce astrocytic GR^{KO} in another cohort of ELS mice and subjected them to the two-week running wheel protocol to determine whether the cellular rescue translated to behavioural recovery. Consistent with non-injected naïve and ELS litters (Fig. 1L, M), we observed consistent sexually dimorphic effects of ELS on running wheel behaviour in our control virus-injected (AAV2/5-GfaABC₁D-eGFP) mice with light period hyperactivity in male mice (Fig. 7T–V, Supplementary Fig. 17A) and hypoactivity in female mice (Fig. 7W–Y, Supplementary Fig. 16B). In agreement with the cellular data, we report that astrocytic GR^{KO} in the LH rescued the effects of ELS on running wheel behaviour, diminishing light period hyperactivity in male ELS mice (Fig. 7V) and restoring distance ran per day in female ELS mice (Fig. 7X). Taken together, these data support the hypothesis that astrocytic GR signalling mediates the effects of ELS in the LH disrupting the excitability of orexin neurons to perturb diurnal activity rhythms in a sex-specific manner.

Discussion

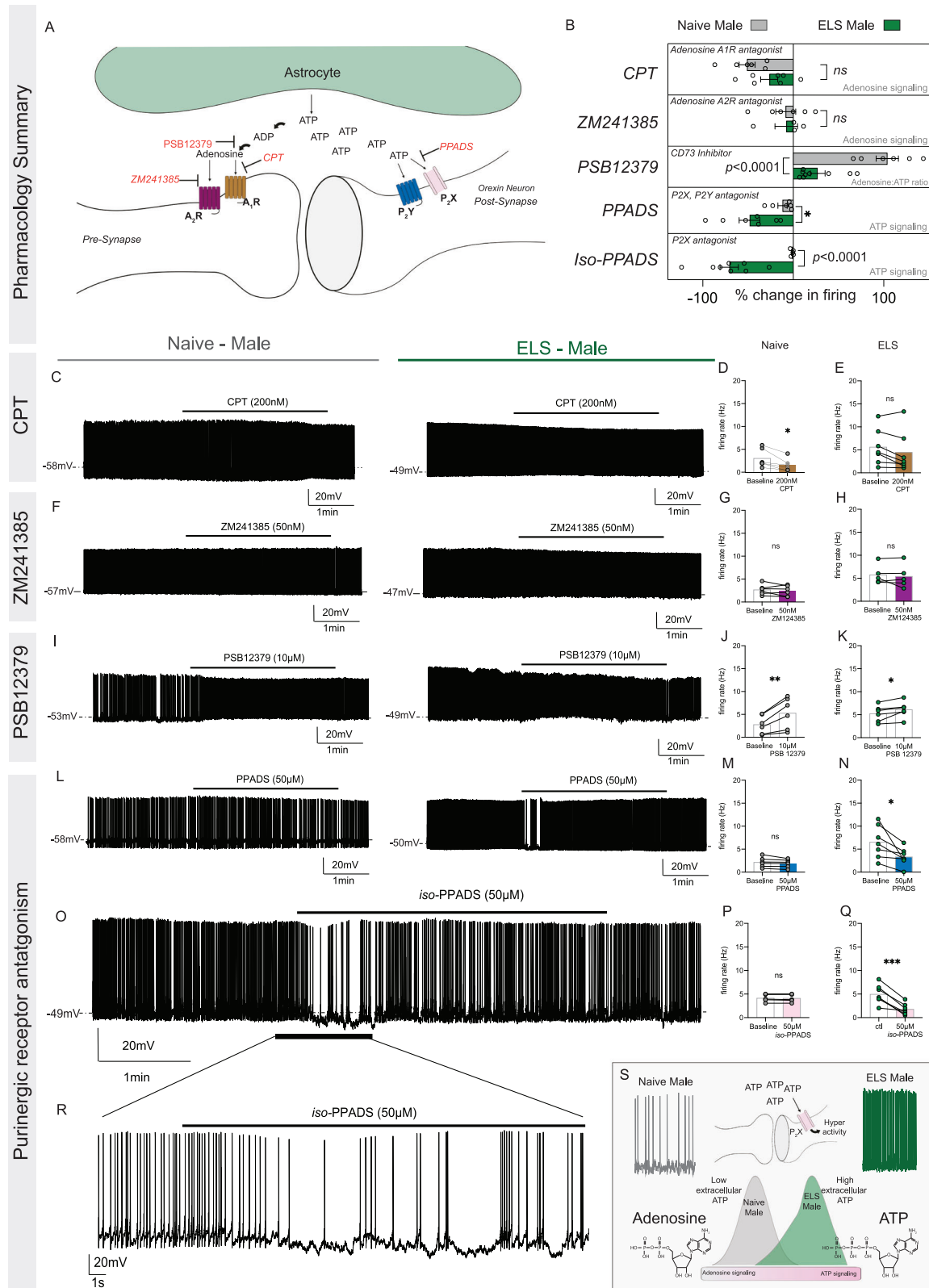
In this study, we investigated the contribution of astrocytes in stress-induced behavioural change. We show that astrocytic stress signalling drives the cellular and behavioural effects of early-life stress on lateral hypothalamus-dependent behaviour in a sex-specific manner. Using an ELS paradigm shown to prompt long-term cellular and behavioural deficits, we report a strong sexual dimorphism in stress-induced activity changes with hypoactivity in female and hyperactivity in male mice accompanied by increased blood glucocorticoid levels in both sexes. Focusing on the lateral hypothalamus, we observed reorganisation of astrocytic morphology, downregulation of key astrocytic proteins, and disruption of spontaneous firing of orexin neurons. Importantly, we show that manipulating astrocyte function alone is sufficient to perturb orexin neuron firing rates and diurnal patterns of wheel running using a chemogenetic strategy. We found orexin neuron firing abnormalities caused by ELS were driven by distinct mechanisms, with elevated purinergic signalling in ELS male mice, and reduced L-lactate availability in ELS female mice. Considering increased glucocorticoid levels was a conserved phenotype between sexes, we tested whether targeting this pathway could alleviate the effects of stress on cellular and behavioural scales. Using transgenic mice to induce an

astrocyte-specific downregulation of glucocorticoid receptors in the lateral hypothalamus, we reveal that glucocorticoid signalling in astrocytes is necessary for the effects of ELS on cellular pathology, aberrant firing patterns of orexin neurons, and wheel running behaviour in both female and male mice.

The precise ELS model employed in this study has been shown to have a wide influence on transcriptomic profiles in both cortical and sub-cortical brain regions, with distinct sexual dimorphism in the transcriptional response to ELS³⁷. In agreement, we report sex differences at both behavioural and cellular scales. We focused our work on lateral hypothalamic astrocytes and their control of LH-specific behaviours however, ELS exerts a strong influence on behaviour *via* pleiotropic effects across multiple brain regions including the amygdala, PFC, striatum^{40,114}. While we failed to observe a change of running wheel measures in constant darkness, investigation of running wheel adaptation over longer period of total darkness would give insight into the long-term effects of ELS on SCN generated rhythms. Given prolonged circadian perturbation and early-life stress (or adversity) are among the strongest risk factors associated with the development of anxiety and depression¹¹⁵ understanding the cellular mechanisms and what makes stress during development so profound is essential.

As almost all brain cells express the *nr3c1* gene that codes for the glucocorticoid receptor¹¹⁶, as such the elevated blood corticosterone levels at P45 that we show and any subsequent signalling in the CNS are bound to have widespread effects. It would be of great interest to understand the specific contribution of GR signalling in other glial cell types^{117,118} and in neurons to determine their respective contributions to ELS-induced behavioural change. One reason why we believe astrocytes are particularly sensitive to glucocorticoids is due to the proximity of astrocytic endfeet to brain cerebrovasculature¹¹⁹, the entry point of blood glucocorticoids to the brain parenchyma enabling them to coordinate synaptic signals with signals from the vasculature¹²⁰ including changes in circulating glucocorticoids. Indeed, RNA-seq data suggests a 7-fold higher expression of *nr3c1* in astrocyte (28.5 FPKM) compared to neurons (3.75 FPKM)¹¹⁶, so we postulate astrocytes are spatially and transcriptionally poised as primary mediators of the central effects of glucocorticoids. This notion is supported by the data presented here which reveals astrocytic GR signalling as a key mediator of the effects of early-life stressors. This emphasises the need for further understanding of astrocytic GR signalling in both physiological and pathological conditions.

Given that local (LH-specific) deletion of astrocytic GR signalling corrected the sex-specific effects of ELS on both orexin neuron firing rates and behaviour, we propose the mechanism underlying ELS originates from a common dysfunction of astrocytes with sex differences downstream of initial glucocorticoid signalling. Given the high level of transcriptomic heterogeneity in male and female astrocytes across the



developmental period¹², it is conceivable that epigenetic changes induced by ELS are also distinct in male and female astrocytes. On the protein level, the observed reduction in GFAP and Cx43 in ELS mice was more pronounced in female mice. In this context female astrocytes display a hypofunctional phenotype whereas males exhibit hyperfunction with elevated gliotransmission. Considering ELS induced levels of corticosterone were identical between the sexes and

that deletion of GR in astrocytes corrected neuronal firing and behavioural phenotypes in both sexes, these data support the hypothesis that astrocytic GR activation induces distinct cellular responses between sexes.

We observed important sex differences in the neuronal response to ELS. A noteworthy finding from our patch-clamp experiments is that both male and female ELS orexin neurons display a persistent

Fig. 5 | Elevated P2X receptor signalling drives increased firing rates in male ELS mice. **A** Schematic of orexin neuron tripartite synapse and overview of mechanism of action of pharmacological agents. **B** Percentage change in firing after bath application of modulators of the purinergic system. two-way ANOVA; Uncorrected Fisher's LSD: 8-cyclopentyltheophylline (CPT) ($p = 0.0786$, Naïve $N = 2$, $n = 6$ cells, ELS $N = 2$, $n = 7$ cells), ZM-241385 ($p = 0.973$, Naïve $N = 2$, $n = 6$ cells, ELS $N = 3$, $n = 5$ cells), PSB12379 ($p < 0.001$, Naïve $N = 2$, $n = 6$ cells, ELS $N = 3$, $n = 6$ cells), PPADS ($p = 0.0102$, Naïve $N = 2$, $n = 6$ cells, ELS $N = 3$, $n = 7$ cells), iso-PPADS ($p < 0.001$, Naïve $N = 3$, $n = 5$ cells, ELS $N = 3$, $n = 7$ cells). **C** Representative traces of orexin neurons from Naïve and ELS male mice before and after bath application of adenosine A1 receptor antagonist, CPT (200 nM). **D** Change in firing rate in Naïve mice with application of adenosine A1 receptor antagonist, CPT (Paired *t* test: baseline = 3.035, ± 0.822 , CPT (200 nM) = 1.56 ± 0.564 , ($N = 2$, $n = 6$ cells) $p = 0.0178$). **E** Change in firing rate in ELS mice with application of CPT (Paired *t* test: baseline = 5.60 Hz ± 1.47 , CPT = 4.44 Hz ± 1.69 ($N = 2$, $n = 7$ cells) $p = 0.068$). **F** Representative traces of orexin neurons from Naïve and ELS male mice before and after bath application of adenosine A2 receptor antagonist, ZM241385 (50 nM). **G** Change in firing rate in Naïve mice with ZM241385 (Paired *t* test: baseline = 2.671 Hz ± 0.461 , ZM241385 = 2.422 Hz ± 0.468 ($N = 2$, $n = 6$ cells) $p = 0.448$). **H** Change in firing rate in ELS mice with application of adenosine A2 receptor antagonist, ZM241385 (Paired *t* test: baseline = 5.756 Hz ± 0.938 , ZM241385 = 5.421 Hz ± 1.15 ($N = 3$, $n = 5$ cells) $p = 0.528$). **I** Representative traces of orexin neurons from Naïve and ELS male mice

before and after bath application of Ecto-5'-Nucleotidase (CD73) inhibitor, PSB12379 (10 μ M). **J** Change in firing rate in Naïve mice with PSB12379 (Paired *t* test: baseline = 2.78 Hz ± 0.826 , PSB12379 = 5.29 Hz ± 1.39 ($N = 2$, $n = 6$ cells) $p = 0.0086$). **K** Change in firing rate in ELS mice with PSB12379 (Paired *t* test: baseline = 5.23 Hz ± 0.720 , PSB12379 = 6.105 Hz ± 6.11 ($N = 3$, $n = 6$ cells) $p = 0.029$). **L** Representative traces of orexin neurons from Naïve and ELS male mice before and after bath application of PPADS tetrasodium salt (50 μ M). **M** Change in firing rate in Naïve mice with PPADS (Paired *t* test: baseline = 2.13 Hz ± 0.440 , PPADS = 1.88 Hz ± 0.361 ($N = 2$, $n = 6$ cells) $p = 0.111$). **N** Change in firing rate in ELS mice with PPADS (Paired *t* test: baseline = 6.52 Hz ± 1.34 , PPADS = 3.32 Hz ± 0.737 ($N = 3$, $n = 7$ cells) $p = 0.025$). **O** Representative trace of orexin neurons from ELS male mice before and after bath application of P2X purinoreceptor antagonist, iso-PPADS tetrasodium salt (50 μ M). **P** Change in firing rate in Naïve mice with iso-PPADS (Paired *t* test: baseline = 4.13 Hz ± 0.368 , iso-PPADS = 4.09 Hz ± 0.377 ($N = 3$, $n = 5$ cells) $p = 0.237$). **Q** Change in firing rate in ELS mice with iso-PPADS (Paired *t* test: baseline = 4.96 Hz ± 0.759 , iso-PPADS = 1.77 Hz ± 0.448 ($N = 3$, $n = 7$ cells) $p = 0.006$). **R** Zoom in representative trace after application of iso-PPADS. **S** Schematic highlighting shift in extracellular adenosine to ATP in ELS male mice. Extracellular ATP signalling through P2X receptors on the post-synaptic membrane to induce elevated spontaneous firing rates in orexin neurons. N = mice, n = cells. Bar charts = mean \pm S.E.M. ns = not significant, $^*p < 0.05$, $^{**}p < 0.01$.

depolarisation of the RMP, yet ELS has opposing effects of firing rates, driving behaviour. We explored the contribution of purinergic signalling in our neuronal firing phenotype observed in ELS male mice. Consistent with previous work⁵³, we found ATP had an excitatory effect on orexin neuron activity, with P2X receptor activity driving the elevated firing rates in males. In females however, we observed attenuation of firing rates which was rescued upon supplementation with 5 mM L-lactate. Previous research demonstrated L-lactate maintains the firing frequency of orexin neurons by fuelling ATP sensitive potassium channels (K_{ATP})^{55,56}. As we report a depolarisation of the RMP (Fig. 2) with a restoration of firing rate and not RMP upon L-lactate application, we posit that the corrective effects of L-lactate more likely involve restoration of ATP sensitive metabolic pathways for action potential generation rather than direct modulation of resting ion conductances.

Our ELS paradigm coincides with peak astrocyte process outgrowth and integration with synaptic elements (P14-21), which could explain the atrophic morphological phenotypes observed in both ELS male and female astrocytes in the LH¹³. Furthermore, there is evidence for differences in gene expression profiles across post-natal development between male and female astrocytes¹². This could explain the more pronounced effect of ELS on female astrocyte morphology compared to males, where female astrocytes exhibit an arrested development as a consequence. Therefore, it is plausible that this ELS paradigm functions as a “two-hit susceptibility hypothesis”, where ELS alters post-natal development of astrocyte morphology (Hit 1 – *primer*). Stress-induced elevations in glucocorticoids activate signalling pathways that result in dysfunctional astrocyte-synapse interactions and subsequent behavioural maladaptation (Hit 2 – *effector*). To definitively test whether disrupted astrocyte morphology in ELS is one of the main drivers and/or primers of the synaptic and behavioural dysfunction, the field requires more precise tools to manipulate astrocyte morphology in real-time and measure the effects on brain circuits underlying behaviour.

Globally, our work contributes to the growing body of literature demonstrating the important role of glial cells in behavioural regulation and how this can be perturbed in pathology. Showing that astrocyte dysfunction is both necessary and sufficient to drive stress-induced behavioural change, our work supports a shift in how to conceptualise the cellular and molecular mechanisms of stress. Indeed, the responsiveness of astrocytes to hormonal cues is not limited to glucocorticoids but has also been shown for insulin¹²¹⁻¹²³, leptin¹²⁴, and ghrelin¹²⁵. Disruption of these hormone signalling

pathways in astrocytes also affected behaviour including wheel running activity¹²¹. Together these independent observations underscore the important role of astrocytes in contextual guidance of neural circuits¹²⁶, whereby astrocytic integration of both hormonal and synaptic information is key to adaptation. Our findings pave the way to a more comprehensive incorporation of astrocyte biology in behavioural neuroscience, towards multicellular models of brain function.

Methods

Animals

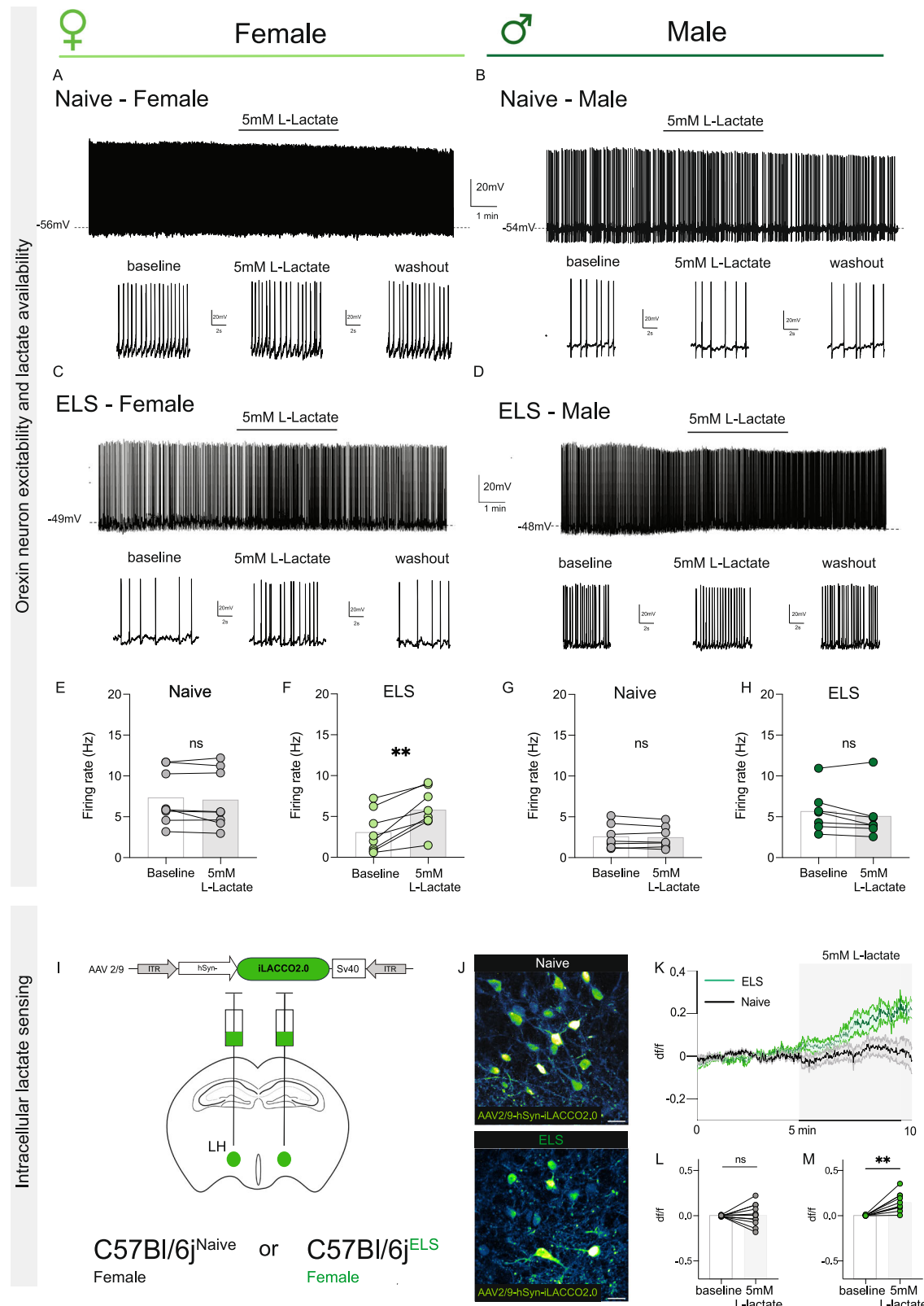
All experiments were performed in accordance with the guidelines for maintenance and care of animals of the Canadian Council on Animal Care (CCAC) and approved by the Institutional Committee for the Protection of Animals (CIPA) at the Centre Hospitalier de l'Université de Montréal, protocol number CM24041CMRs. Both male and female C57BL/6J mice (Jax #000664) and Nr3c1^{f/f} (Jax # 021021) were used in the study, housed on a 12 h:12 h light:dark cycle (lights on at 06:30) with *ad libitum* access to food (Teklad Irradiated Global 18% Protein Rodent Diet) and water.

Early life stress protocol

C57BL/6J or Nr3c1^{f/f} pups were separated from their mothers for 4-h per day (ZT2-ZT6) between post-natal days 10 and P17. During separation pups and mothers were placed into new cages with 70% less bedding. Bedding was weighed on P10 and divided into each cage (home cage, pup separation cage, and mother separation cage). Separated pups and mothers had *ad libitum* access to food and water and pup cages were placed on a water heating pad maintained at 34 °C. After the final day of separation (P17) bedding was returned to the original amount and pups were housed with their mothers until weaning at P21.

Behavioural assays

2-week running wheel protocol. Mice aged P45-P55 were single housed with a low-profile wireless running wheels (Med Associates, NV-047 & 047V) for 2 weeks (1 week habituation, 1 week data acquisition). Mice were undisturbed for the 2 weeks with *ad libitum* access to food and water. Total distance was calculated with an inhouse MatLab script using ZT binned revolutions per day and running wheel circumference ($2 \times \pi \times r$). Light period activity counts were averaged across 3 days during data acquisition (days 9-11). Curve analysis for 24-hour activity cycles were calculated from extracted 5-min bin data and the following measures were quantified; Area Under the Curve (AUC),



Peak wheel running, and Full-Width at Half-Max (FWHM). COSINOR analyses were run on 5 days of running wheel rhythms from day 10-15 of week 2.

Sucrose Preference Test (SPT). Mice were housed with dual-water bottle AllenTown cages, for 48 hours with two bottles containing water (switched at 24 hours) to account for novelty induced water intake.

Bottles were next replaced with either water or a 1% sucrose solution for 2 days, which were switched at 24 hours after sucrose presentation. Sucrose preference ratios were calculated using the following equation.

$$\frac{1\% \text{ sucrose}}{\text{Water} + 1\% \text{ sucrose}} = \text{Sucrose preference ratio (\%)}$$

Fig. 6 | ELS disrupts extracellular Lactate availability in female mice.

A–D Representative trace of orexin neuron firing from (A) Naïve female, (B) Naïve male, (C) ELS female, (D) ELS male before and during bath application of 5 mM L-Lactate. **E** Absence of change in firing rate in Naïve female mice with 5 mM L-Lactate (Paired *t* test: baseline = 7.36 Hz \pm 1.18, 5 mM L-Lactate = 7.10 Hz \pm 1.27 (N = 3, n = 8 cells) p = 0.311). **F** Increase in firing rate in ELS female mice with 5 mM L-Lactate (Paired *t* test: baseline = 3.08 Hz \pm 0.898, 5 mM L-Lactate = 5.83 Hz \pm 0.911 (N = 3, n = 8 cells) p = 0.0014). **G** Absence of change in firing rate in Naïve male mice with 5 mM L-Lactate (Paired *t* test: baseline = 2.61 Hz \pm 0.583, 5 mM L-Lactate = 2.50 Hz \pm 0.517 (N = 3, n = 7 cells) p = 0.354). **H** Absence of change in firing rate in ELS male mice with 5 mM L-Lactate (Paired *t* test: baseline = 5.70 Hz \pm 1.00, 5 mM L-Lactate = 5.10 Hz

\pm 1.14 (N = 3, n = 8 cells) p = 0.113). **I** Injection of fluorescent intracellular L-Lactate sensor into neurons in the LH of Naïve and ELS female mice. **J** Representative images of iLACCO2.0 expressing neurons in acute slices of the LH, scale bars = 25 μ m. **K** Change in normalised fluorescence intensity (df/f) of iLACCO2.0 before and during 5 min of bath application of 5 mM L-Lactate. **L** Change in df/f of in Naïve female neurons expressing iLACCO2.0 (paired *t* test: baseline = -0.0017 df/f \pm 0.00191, 5 mM L-Lactate = 0.0075 df/f \pm 0.0331 (N = 3, n = 12 cells) p = 0.778). **M** Change in df/f of in ELS female neurons expressing iLACCO2.0 (paired *t* test: baseline = 0.0040 df/f \pm 0.00157, 5 mM L-Lactate = 0.1495 df/f \pm 0.0323 (N = 3, n = 10 cells) p = 0.0012). **N** = mice, **n** = cells. Bar charts = mean \pm S.E.M. ns = not significant, * P < 0.05, ** P < 0.01.

Body composition

Fat and lean mass was assessed using a nuclear echo magnetic resonance imaging (EchoMRI) whole-body composition analyser as were previously described¹²⁷.

Metabolic cages

Parameters of energy balance, including respiratory exchange ratio (RER), energy expenditure, and locomotor activity were measured by indirect calorimetry in Comprehensive Lab Animal Monitoring System metabolic cages (CLAMS, Columbus Instruments International, Columbus, OH, USA). Mice were single housed in CLAMS cages at 21 ± 0.2 °C in a dark-light cycle for 24 hour to acclimate before measurements. Energy balance parameters were measured for 48 hours. Energy expenditure was normalised by lean mass.

Blood collection and corticosterone analysis

Trunk blood was collected *via* rapid decapitation at ZT2 (08:30) or ZT14 (20:30). To minimise handling-induced elevations in corticosterone mice were housed with clear plastic tubes used to move individual mice into an enclosed chamber filled with 5% isoflurane for 2 min. Mice were placed in enclosed Isoflurane chambers until loss of toe pinch reflex (maximum elapsed time of 2 min). Mice were decapitated and trunk blood was collected into BD 365963 Microtainer® Capillary Blood Collection Tubes and placed onto Ice. Blood was centrifuged for 7 min at 4 °C at 2380 \times g. Serum was aliquoted and stored at -80 °C. Corticosterone measurements were obtained using an ENZO ELISA kit (ADI-900-097).

Acute brain slice preparation

Coronal slices containing lateral hypothalamus were obtained from mice between P45-60 at hours 08:00–10:00 am (ZT2-4). Animals were anaesthetised with isoflurane and the brain was rapidly excised and placed in ice-cold NMDG based cutting solution saturated with 95% O₂ and 5% CO₂ containing the following (in mM): 119.9 NMDG, 2.5 KCl, 25MgCl₂, 1 CaCl₂, 1.4 NaH₂PO₄ and 20 D-glucose saturated with 95% O₂ and 5% CO₂. Slices (250 μ m thick) were cut on a vibratome (Leica VT1200, Nussloch, Germany). Slices were transferred to oxygenated NMDG cutting solution artificial CSF (aCSF) at 33 ± 0.5 °C for 15 min followed by a 1-hour recovery period in artificial CSF (aCSF) at RT containing the following (in mM): 130 NaCl, 2.8 KCl, 1.25 NaH₂PO₄, 1.2 MgCl₂, 2.5 CaCl₂, 2.5 Glucose, 300-305 mOsmol. For experiments, slices were transferred to a recording chamber where they were perfused (2 ml/min) with aCSF at RT for the course of the experiment. Slices were used for a maximum of 5 hr after cutting.

Electrophysiology

Orexin neurons in the LH were identified through positive expression of AAV2/8-miniHCRT-TdTomato with a plan n 4x/0.10 magnification (Olympus) or LUMPlanFL N 40x/0.80 magnification (Olympus) objective with an upright scicam pro camera (Scientifica). Whole-cell patch-clamp recordings of orexin neurons were performed in current- and voltage-clamp configuration. Recordings were made at room

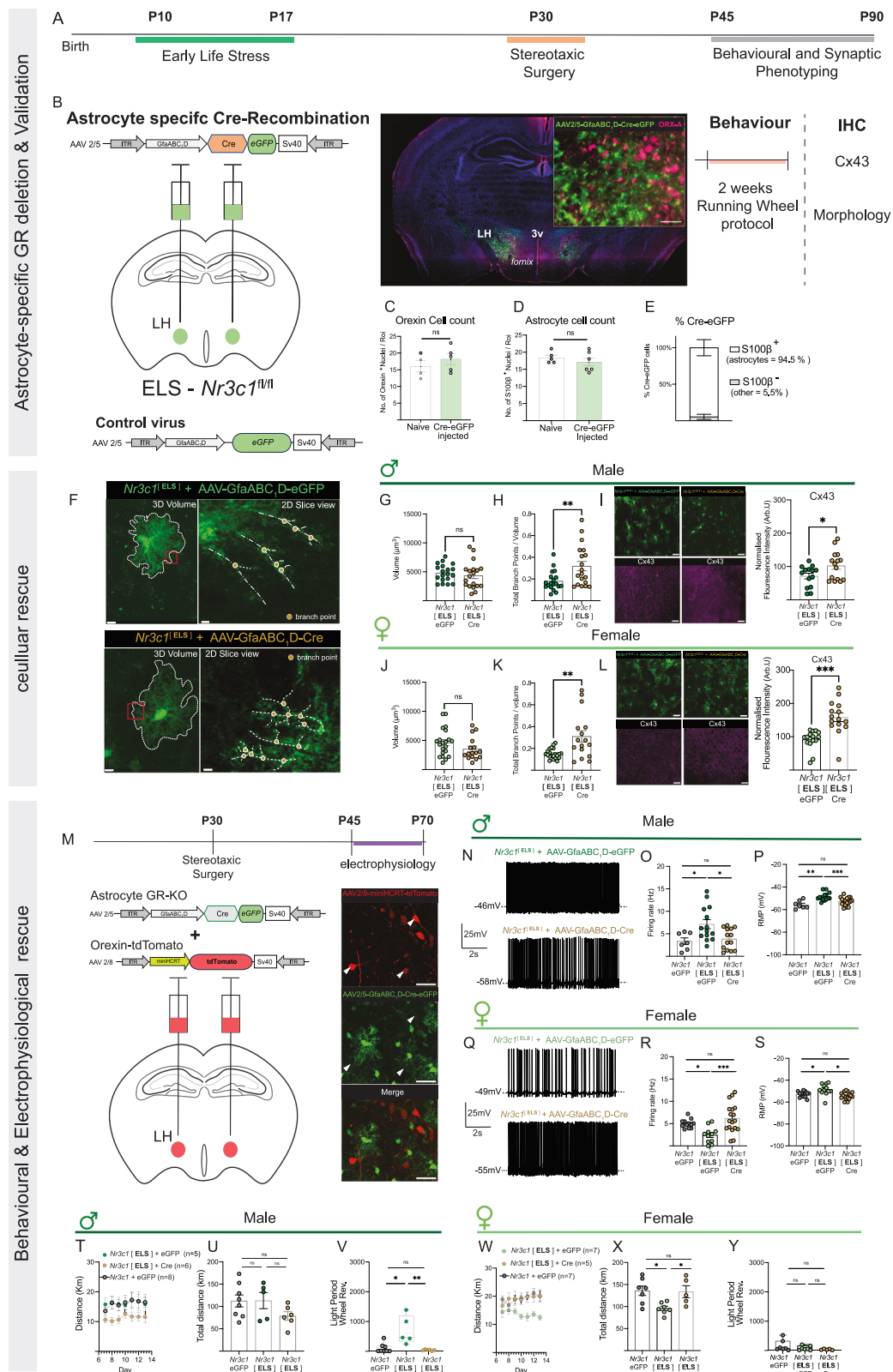
temperature. Data were acquired using a Multiclamp 700B amplifier (Molecular Devices) and digitised using a Digidata 1440A digitiser and pClamp/Clampfit 10.7 (Molecular Devices). Pipettes (from borosilicate capillaries; World Precision Instruments) had resistances of 4-8 mega-ohms and were filled with an internal solution containing the following (in mM): 105 K-gluconate, 30 KCl, 10 phosphocreatine, 4 ATP-Mg, 0.3 GTP-Tris, 0.3 EGTA (adjusted to pH7.2 with KOH; 290-300 mOsmol). For AAV2/8-miniHCRT-TdTomato validation experiments biocytin (2 mg/mL; Sigma) was added to the internal solution. All recordings were analysed with Clampfit 10.2 and 10.6 from pClamp software (Molecular Devices) and EasyEphys software. Liquid Junction Potentials were not adjusted for. Recordings were discarded if access resistance (Ra) values changed by more than 30% across recording time and/or whole-cell patch clamp recordings had Ra values higher than 25 mega-ohms. The action potential firing rate was calculated by automated analysis through Clampfit 10.2. Excitatory Post-Synaptic Potentials (EPSCs) were obtained in the voltage-clamp configuration (-70 mV) for 2 min. For Inhibitory Post-Synaptic Potentials (IPSCs) pipettes were filled with an internal solution containing the following (in mM): 130 CsCl, 10 NaCl, 1 EGTA, 0.1 CaCl₂, 10 PCr, 4 ATP-Mg, 0.4 GTP-Na, 5 QX-314 (adjusted to pH7.2 with KOH; 290-300 mOsmol). IPSC recordings were obtained in the voltage-clamp configuration (-70 mV) for 2 min with 20 μ M of DAP-5 (Tocris, 0106) and 30 μ M of DNQX (Tocris, 0189) in the aCSF. For all EPSC and IPSC analyses, experimenters were blinded when scoring traces by hand. Input resistance (R_{in}) was determined by measuring the slope of the linear portion of the current-voltage (I-V) curve.

Pharmacology

Adenosine A1 receptor antagonist, 8-Cyclopentyl-1,3-dimethyl-xanthine (Tocris, 6137). Adenosine A2 receptor antagonist, ZM 241385 (Tocris, 1036). Ecto-5'-nucleotidase CD73 inhibitor, PSB-12379 (Tocris, 6083). Purinergic 2 receptor antagonist, PPADS tetrasodium salt (Tocris, 0625), and purinergic 2X receptor antagonist, *iso*-PPADS tetrasodium salt (Tocris, 0683).

Two-photon imaging

Fluorescence intracellular lactate imaging was performed with a custom two-photon laser-scanning microscope (Scientifica). The microscope was equipped with a Ti:Sapph laser (Ultra II, Coherent), a green bandpass emission filter (525–40 nm), an orange/red bandpass emission filter (605–70 nm), and associated photomultiplier tubes (GaAsP, Hamamatsu). Time-series images were acquired through bidirectional laser scanning (920 nm excitation laser, 86.85 μ m \times 86.85 μ m, 512 \times 512 pixels at 1 Hz) at a single focal plane incorporating a cluster of neurons expressing AAV2/9-hSyn-iLACCO2.0. All images were acquired using Scanimage (mbf bioscience). Acute brain slices (250 μ m thick) containing the lateral hypothalamus were obtained from mice between ages P45-55). Animals were anaesthetised with isoflurane and the brain was rapidly excised and placed in ice-cold NMDG based cutting solution saturated with 95% O₂ and 5% CO₂ containing the following (in mM): 119.9 NMDG, 2.5 KCl, 25MgCl₂, 1 CaCl₂, 1.4 NaH₂PO₄ and 20 D-glucose saturated with 95% O₂ and 5% CO₂.



D-glucose saturated with 95% O₂ and 5% CO₂. Slices (350 μ m thick) were cut on a vibratome (Leica VT1200, Nussloch, Germany). Slices were transferred to oxygenated NMDG cutting solution artificial CSF (aCSF) at 33 \pm 0.5 °C for 15 min followed by a 1-hour recovery period in artificial CSF (aCSF) at RT containing the following (in mM): 130 NaCl, 2.5 KCl, 1.25 NaH₂PO₄, 26 NaHCO₃, 2.5 glucose, 1.3 MgCl₂, 2 CaCl₂, pH

7.2–7.3 and 300–305 mOsmol. All time-series images were acquired in a recording chamber constantly perfused with aCSF as described above. We conducted 5 min of baseline imaging before another 5 min with bath application of 5mM L-lactate (Sigma, 71718-10 G). ImageJ was used to analyse individual soma of AAV2/9-hSyn-iLACCO2.0- expressing neurons to calculate df/f.

Fig. 7 | Astrocyte specific deletion of glucocorticoid receptors (GR) in the LH corrects cellular and behavioural impairments induced by ELS. **A** Experimental timeline for combined ELS and genetic deletion of astrocyte GRs in the LH. Separate cohorts of mice subjected to behavioural protocols or IHC. **B** Viral construct used to achieve astrocyte specific deletion of GR receptors in *Nr3c1*/fl mouse line, scale bar = 25 μ m. **C–E** Validation of AAV2/5-GfaABC₁D-Cre-eGFP expression in LH astrocytes. **C** quantification of orexin neurons (Mann–Whitney test: Naïve = 16 cells \pm 1.77, (N = 4), Cre-eGFP injected = 19 cells \pm 1.66 (N = 5), p = 0.381), **(D)** Quantification of S100 β astrocytes (Mann–Whitney test Naïve = 17 cells \pm 1.20 (N = 6), Cre-eGFP injected = 18.40 cells \pm 0.759 (N = 5), p = 0.495), **(E)** Cellular identity of Cre-eGFP and expression specificity of 94.5% in S100 β + astrocytes (N = 7). **F** Representative LH astrocytes expressing control virus (AAV2/5-GfaABC₁D-eGFP) or AAV2/5-GfaABC₁D-Cre-eGFP in 3D view and 2D slice view of branching structures (branch points & branching processes), 3D volume scalebars = 5 μ m, 2D slice scale bar = 2 μ m. **G** Volume of -eGFP control or cre- expressing LH astrocytes from ELS male mice (unpaired t test: eGFP = 4803 μ m³ \pm 342 (N = 3, n = 19 cells), Cre = 4365 μ m³, \pm 529 (N = 3, n = 19 cells), p = 0.491). **H** Total branch points/volume (unpaired t test: eGFP = 18.18 \pm 2.08 (N = 3, n = 19 cells), Cre = 31.91 \pm 4.30 (N = 3, n = 19 cells), p = 0.007). **I** Normalised Cx43 fluorescence intensity (a.u) in LH of -eGFP control or cre- astrocytes (unpaired t test: eGFP = 71.37Arb.U. \pm 8.56 (N = 3, n = 14 cells), Cre = 102.6Arb.U. \pm 11.1 (N = 3, n = 15 cells), p = 0.036), scale bars = 25 μ m. **J** Volume of eGFP control or cre- expressing LH astrocytes from ELS female mice (Mann–Whitney test: eGFP = 4622 μ m³, \pm 518 (N = 3, n = 21 cells), Cre = 3545 μ m³, \pm 484 (N = 3, n = 16

cells), p = 0.130). **K** Total branch points/volume (unpaired t test: eGFP = 15.15 \pm 0.994 (N = 3, n = 21 cells), Cre = 31.06 \pm 5.27 (N = 3, n = 16 cells), p = 0.0018). **L** Normalised Cx43 fluorescence intensity (a.u) in LH of -eGFP control or cre- astrocytes (unpaired t test: eGFP = 91.32Arb.U. \pm 7.46 (N = 3, n = 15 cells), Cre = 158.5Arb.U. \pm 13.1 (N = 3, n = 15 cells), p < 0.001), scale bars = 25 μ m. **M** Experimental timeline for combined expression of AAV2/5-GfaABC₁D-Cre-eGFP and AAV2/8-miniHCRT-TdTomato in *Nr3c1*-ELS mice, scale bars = 25 μ m. **N** Representative firing rates of orexin neurons in Naïve eGFP (N = 3, n = 7), ELS eGFP (N = 3, n = 14) and ELS Cre (N = 3, n = 14) injected male mice. **O** Restoration of RMP (one-way ANOVA: F = 10.32, p < 0.001) and **(P)** firing rates (one-way ANOVA: F = 5.78, p = 0.0072) in Naïve eGFP (N = 3, n = 7), ELS eGFP (N = 3, n = 14) and ELS Cre (N = 3, n = 17) injected male mice. **Q** Representative firing rates of orexin neurons in Naïve eGFP (N = 3, n = 12) ELS eGFP (N = 3, n = 11) and ELS Cre (N = 3, n = 18) injected female mice (one-way ANOVA: F = 7.90, p = 0.0014). **R** Restoration of RMP (one-way ANOVA: F = 7.90, p = 0.0014) and **(S)** firing rate (one-way ANOVA: F = 8.32, p = 0.001) in Naïve eGFP (N = 3, n = 11), ELS eGFP (N = 3, n = 12), and ELS Cre (N = 4, n = 16) injected female mice. **T**, **V** Running wheel behaviour of eGFP and Cre injected male mice: **(T)** Distance ran per day, **(U)** Total distance (one-way ANOVA: F = 1.96, p = 0.173), and **(V)** Light cycle activity (one-way ANOVA: F = 3.23, p = 0.001). **W**–**Y** Running wheel behaviour of eGFP and Cre injected female mice: **(W)** Distance ran per day, **(X)** Total distance (one-way ANOVA: F = 6.02, p = 0.01), and **(Y)** Light cycle activity (one-way ANOVA: F = 1.24, p = 0.315). N = mice, n = cells. Bar charts = mean \pm S.E.M. ns = not significant, * P < 0.05, ** P < 0.01, *** P < 0.001.

Stereotaxic surgery

P30 mice were given a subcutaneous (s.c.) injection of Carprofen (20 mg/kg) minimum 1 h prior to surgery. Animals were deeply anaesthetised (5% isoflurane) before placing them into a stereotaxic frame (maintained with 1-2% isoflourane) (*Kopf instruments*). The surgical site was infiltrated with bupivacaine/lidocaine (2 mg/kg sc.) 10 min prior surgery. Two small holes were made to bilaterally expose the brain surface under the skull. A 10 μ L Neuro syringe (Hamilton) was filled with the following AAV constructs produced at the Canadian Neurophotonics Viral Vector Core (RRID: SCR_016477): AAV2/5-gfaABC₁D-eGFP (1.5 \times 10^{11–12} GC/ml), AAV2/5-gfaABC₁D-Cre-eGFP (1.5 \times 10¹² GC/ml), AAV2/5-MiniHCRT-TdTomato (7.0 \times 10¹² GC/ml), AAV2/5-gfaABC₁D-HM3d(Gq)-mCherry (1.5 \times 10¹² GC/ml), AAV2/5-gfaABC₁D-HM4d(Gi)-mCherry (1.5 \times 10¹² GC/ml), AAV2/5-gfaABC₁D-mCherry (1.5 \times 10¹² GC/ml), AAV2/9-hSyn-iLACCO2.0 (1.5 \times 10¹³ GC/ml). 600 nl of vector per hemisphere was injected at 200 nL/min into the lateral hypothalamic area (AP/DV/ML = \pm 1.6/–5.3/±0.9 mm) using a micro-injection syringe pump (UMP3T-2 World Precision Instruments). For morphological analysis of astrocytes in the LHa viral titres were dropped ten-fold to 10¹¹ GC/ml. Mice were given minimum 2 weeks to recover from surgeries before experiments.

Chemogenetics

Male and female mice injected with either AAV2/5-gfaABC₁D-HM3d(Gq)-mCherry, AAV2/5-gfaABC₁D-HM4d(Gi)-mCherry, or AAV2/5-gfaABC₁D-mCherry were singly housed for two weeks with running wheels (Methods: *2 week running wheel protocol*). Water intake was measured for the three last days of week 1 (days 4–7). Clozapine-N-Oxide (CNO) (Tocris, #4936) was standardised to body weight on day 7 and water intake averaged across days 4–7 and delivered into the drinking water for 3 days. CNO was delivered to mice at 1.25 mg/Kg, 2.5 mg/Kg, and 5 mg/Kg. For Morphological analyses mice were rapidly perfused at ZT0 (lights off).

Brain processing

Mice were anaesthetised in an enclosed chamber filled with isoflurane (5% for induction, 3–4% for maintenance, v/v) until loss of toe pinch reflex. All perfusions occurred between ZT2–4. A transcardial perfusion was used to ensure uniform preservation of tissue and brains were fixed in 4% paraformaldehyde (PFA) for 24 h at 4 °C. The fixed brains were then placed in 15 ml falcon tubes containing 30% sucrose solution for a minimum of two days. Brains were embedded in optimal cutting

temperature (OCT) compound and flash frozen in 2-methylbutane between –40 and –50 °C and then stored at –80 °C until cryo-sectioning. Brains were cut at 35 μ m thickness at –20 °C using a Leica CM3050S Cryostat. Slices were stored in a cryoprotector solution at 4 °C until immunohistochemistry.

Immunohistochemistry

Free floating brain slices were washed 3 times in 1X PBS for 15 min to remove cryoprotector solution. Slices were permeabilised in block-perm solution (3% Bovine-Serum-Albumin, 0.5% Triton^{10%} in PBS) for a duration of 1 hour. Slices were incubated with antibodies for 24 h at 4 °C. Slices were incubated with primary antibodies selected based on validation in previous literature; [rabbit] anti-S100 β (1:1000, Abcam, ab52642), [Mouse] anti-glucocorticoid receptor (1:500, ThermoFisher, MA1-510), [chicken] anti-GFAP (1:1000, ThermoFisher, PA1-10004), [mouse] anti-Cx43 (1:1000 ThermoFisher, 3D8A5), [mouse] anti-orexin-A (1:1000, NovusBio, MAB763) and [rabbit] anti-eGFP (1:500, ThermoFisher, G1362), [mouse] anti-NeuN (1:250, Novus. Bio, NBP1-77686), [rabbit] anti-Glutamine Synthetase (1:500, Abcam, ab73593), [rabbit] anti-Cre (1:500, Synaptic Systems, 257 003). After primary antibody incubation slices were washed 3 times in 1X PBS for 15 min to remove non-specific binding. Slices were incubated with secondary antibodies in a DAPI solution (1:10000) at RT in aluminium foil for 1 hour. Slices were incubated with secondary antibodies; [goat] anti-rabbit Alexa 488 (1:1000, Jackson Immuno Research, 111-545-144), [goat] anti-mouse Alexa 647 (1:1000, ThermoFisher, A32728), [goat] anti-chicken Alexa 568 (1:1000, ThermoFisher, A11041). After secondary antibody incubation slices were washed again 3 times in 1X PBS for 15 min before being mounted onto Fisherbrand microscope slides using ProLongTM Glass Antifade mountant (P36982).

Microscopy

Slices were imaged using a Leica TCS SP5 laser scanning confocal microscope with oil immersion Plan-Apochromat 63x objective 1.4 NA,. 16-bit images of 246 \times 246 μ m areas were acquired at 400 Hz (frame size (x*y): 1024 \times 1024, pixel size: 250 nm). 25–30 μ m z-stacks were acquired with a step size of 0.5 μ m. 15 μ m max intensity z-projections of the lateral hypothalamus were analysed using ImageJ (Fiji) to obtain Arb.U. fluorescence intensity measures of secondary antibodies attached to primaries with specificity to epitopes; GFAP, Cx43, and GR. We centred astrocytes with a 2241.025 μ m² ROI and applied a fluorescence threshold for GFAP and Cx43 fluorescence and

measured integrated density Arb.U. (thresholds; default & Otsu, respectively). Arb.U. measurements were standardised to ROI sizes to obtain normalised fluorescence values. For Astrocytic cell counts S100 β staining masked over DAPI channels and we used the analyse particles function on Fiji, counting the number of DAPI nuclei larger than 10 μm in diameter. Orexin cells were counted manually using the Fiji pointer tool. For nuclear Glucocorticoid Receptor measures, astrocyte (S100 β +) DAPI nuclei were thresholded and used as ROIs for nuclear measures of GR fluorescence (S100 β ⁺ + DAPI⁺).

Astrocyte Morphology. Mice were bilaterally injected with a low titre AAV2/5-gfaABC₁D-eGFP into the LH (Methods: stereotaxic surgery). After 3 weeks mice were transcardially perfused and fixed for immunohistochemistry. To obtain singular astrocytes for morphological reconstruction we imaged astrocytes at injection site periphery regions to limit overlap of eGFP⁺ expressing astrocytes whilst remaining in LH brain territory. Astrocytes were imaged using a LSM laser scanning confocal microscope with oil immersion Plan-Apochromat 63x objective 1.4 NA. 16-bit images of 101.4 \times 101.4 μm areas were acquired at 6 fps (frame size (x \times y); 1724 \times 1724, pixel size; 0.06 μm). 25–30 μm z-stacks were acquired with a step size of 0.5 μm . Isolated astrocytes were reconstructed using the IMARIS platform where we calculated branching, process lengths, 3D volumes, and sholl analyses.

Statistical analyses

Results are presented as mean \pm S.E.M. or box and whisker plots for data with one variable and were analysed with the two-tailed Student's *t* test or Mann–Whitney test, respectively. Chemogenetic experiments used repeated measures *t*-tests to non-parametric equivalents. All data was tested for normality and data sets with more than two conditions were first screened for a Gaussian distribution with Kolmogorov–Smirnov test followed by analysis either with one-way/repeated measures ANOVA or Kruskal–Wallis/Friedman test when needed and Tukey's or Sidak's multiple-comparison parametric post hoc test (data with Gaussian distribution) or by a Dunn's multiple-comparison non-parametric post hoc test (data with non-Gaussian distribution). Diurnal running wheel distances and CLAMS data were analysed using a two-way repeated measures ANOVA. Sample sizes were chosen based on previous literature. Statistical tests are represented with the following significance thresholds, **p* < 0.05; ***p* < 0.01 and ****p* < 0.001. All data were analysed using GraphPad Prism software (Version 9, GraphPad, USA).

Reporting summary

Further information on research design is available in the Nature Portfolio Reporting Summary linked to this article.

Data availability

The data generated in this study have been deposited on the Open Science Framework – <https://doi.org/10.17605/OSF.IO/5R8UX>.

References

- Khakh, B. S. & Sofroniew, M. V. Diversity of astrocyte functions and phenotypes in neural circuits. *Nat. Neurosci.* **18**, 942–952 (2015).
- Verkhratsky, A. & Nedergaard, M. Physiology of Astroglia. *Physiol. Rev.* **98**, 239–389 (2018).
- Perea, G., Navarrete, M. & Araque, A. Tripartite synapses: astrocytes process and control synaptic information. *Trends Neurosci.* **32**, 421–431 (2009).
- Perea, G. & Araque, A. Astrocytes potentiate transmitter release at single hippocampal synapses. *Science* **317**, 1083–1086 (2007).
- Kang, J., Jiang, L., Goldman, S. A. & Nedergaard, M. Astrocyte-mediated potentiation of inhibitory synaptic transmission. *Nat. Neurosci.* **1**, 683–692 (1998).
- Herrera Moro Chao, D. et al. Hypothalamic astrocytes control systemic glucose metabolism and energy balance. *Cell Metab.* **34**, 1532–1547.e6 (2022).
- Olsen, M. L. et al. New insights on astrocyte ion channels: critical for homeostasis and neuron-glia signaling. *J. Neurosci.* **35**, 13827–13835 (2015).
- Lawal, O., Ulloa Severino, F. P. & Eroglu, C. The role of astrocyte structural plasticity in regulating neural circuit function and behavior. *Glia* **70**, 1467–1483 (2022).
- Endo, F. et al. Molecular basis of astrocyte diversity and morphology across the CNS in health and disease. *Science* **378** (2022).
- Schober, A. L., Wicki-Stordeur, L. E., Murai, K. K. & Swayne, L. A. Foundations and implications of astrocyte heterogeneity during brain development and disease. *Trends Neurosci.* **45**, 692–703 (2022).
- Ghézali, G. et al. Connexin 30 controls astroglial polarization during postnatal brain development. *Development* **145** (2018).
- Rurak, G. M. et al. Sex differences in developmental patterns of neocortical astroglia: a mouse transcriptome database. *Cell Rep.* **38**, 110310 (2022).
- Farhy-Tselnicker, I. & Allen, N. J. Astrocytes, neurons, synapses: a tripartite view on cortical circuit development. *Neural Dev.* **13**, 1–12 (2018).
- Qian, K. et al. Revisiting the critical roles of reactive astrocytes in neurodegeneration. *Mol. Psychiatry* **28**, 2697–2706 (2023).
- Valles, S. L. et al. Functions of astrocytes under normal conditions and after a brain disease. *Int. J. Mol. Sci.* **24**, 8434 (2023).
- Vijayan, V. K. et al. Astrocyte hypertrophy in the Alzheimer's disease hippocampal formation. *Exp. Neurol.* **112**, 72–78 (1991).
- Murphy-Royal, C. et al. Stress gates an astrocytic energy reservoir to impair synaptic plasticity. *Nat. Commun.* **11**, 1–18 (2020).
- Naskar, S. & Chattarji, S. Stress elicits contrasting effects on the structure and number of astrocytes in the amygdala versus hippocampus. *eNeuro* **6** (2019).
- Salmon, C. K. et al. Organizing principles of astrocytic nanoarchitecture in the mouse cerebral cortex. *Curr. Biol.* **33**, 957–972.e5 (2023).
- Lau, B. K. et al. Obesity-induced astrocyte dysfunction impairs heterosynaptic plasticity in the orbitofrontal cortex. *Cell Rep.* **36**, 109563 (2021).
- Rodríguez, J. J., Zallo, F., Gardenal, E., Cabot, J. & Busquets, X. Prominent and conspicuous astrocyte atrophy in human sporadic and familial Alzheimer's disease. *Brain Struct. Funct.* **228**, 2103–2113 (2023).
- O'Leary, L. A. & Mechawar, N. Implication of cerebral astrocytes in major depression: a review of fine neuroanatomical evidence in humans. *Glia* **69**, 2077–2099 (2021).
- Roman, C., Vivi, E. & Di Benedetto, B. Morphological features of astrocytes in health and neuropsychiatric disorders. *Adv. Neurobiol.* **26**, 75–92 (2021).
- Oliet, S. H. R., Piet, R. & Poulain, D. A. Control of glutamate clearance and synaptic efficacy by glial coverage of neurons. *Science* **292**, 923–926 (2001).
- Murphy-Royal, C. et al. Surface diffusion of astrocytic glutamate transporters shapes synaptic transmission. *Nat. Neurosci.* **18**, 219–226 (2015).
- Bergles, D. E. & Jahr, C. E. Synaptic activation of glutamate transporters in hippocampal astrocytes. *Neuron* **19**, 1297–1308 (1997).
- Henneberger, C. et al. LTP Induction boosts glutamate spillover by driving withdrawal of perisynaptic astroglia. *Neuron* **108**, 919–936.e11 (2020).
- Ciappelloni, S. et al. Aquaporin-4 surface trafficking regulates astrocytic process motility and synaptic activity in health and autoimmune disease. *Cell Rep.* **27**, 3860–3872.e4 (2019).

29. Sibille, J., Pannasch, U. & Rouach, N. Astroglial potassium clearance contributes to short-term plasticity of synaptically evoked currents at the tripartite synapse. *J. Physiol.* **592**, 87–102 (2014).

30. Djukic, B., Casper, K. B., Philpot, B. D., Chin, L. S. & McCarthy, K. D. Conditional knock-out of Kir4.1 leads to glial membrane depolarization, inhibition of potassium and glutamate uptake, and enhanced short-term synaptic potentiation. *J. Neurosci.* **27**, 11354–11365 (2007).

31. Chever, O., Djukic, B., McCarthy, K. D. & Amzica, F. Implication of Kir4.1 channel in excess potassium clearance: an in vivo study on anesthetized glial-conditioned Kir4.1 knock-out mice. *J. Neurosci.* **30**, 15769–15777 (2010).

32. Theparambil, S. M., Begum, G. & Rose, C. R. pH regulating mechanisms of astrocytes: A critical component in physiology and disease of the brain. *Cell Calcium* **120**, 102882 (2024).

33. Rose, C. R. & Verkhratsky, A. Sodium homeostasis and signalling: The core and the hub of astrocyte function. *Cell Calcium* **117**, 102817 (2024).

34. Pannasch, U. et al. Connexin 30 sets synaptic strength by controlling astroglial synapse invasion. *Nat. Neurosci.* **17**, 549–558 (2014).

35. Chever, O., Pannasch, U., Ezan, P. & Rouach, N. Astroglial connexin 43 sustains glutamatergic synaptic efficacy. *Philos. Trans. R. Soc. Lond. B: Biol. Sci.* **369** (2014).

36. Sancho, L., Contreras, M. & Allen, N. J. Glia as sculptors of synaptic plasticity. *Neurosci. Res.* **167**, 17–29 (2021).

37. Liu, J. H. et al. Distinct roles of astroglia and neurons in synaptic plasticity and memory. *Mol. Psychiatry* **27**, 873–885 (2021).

38. Badia-Soteras, A. et al. Retraction of astrocyte leaflets from the synapse enhances fear memory. *Biol. Psychiatry* **94**, 226–238 (2023).

39. Soto, J. S. et al. Astrocyte Gi-GPCR signaling corrects compulsive-like grooming and anxiety-related behaviors in Sapap3 knockout mice. *Neuron* **0** (2024).

40. Guayasamin, M. et al. Early-life stress induces persistent astrocyte dysfunction associated with fear generalisation. *Elife* **13**, RP99988 (2025).

41. Uy, J. P. & Gotlib, I. H. Associations among early life adversity, sleep disturbances, and depressive symptoms in adolescent females and males: a longitudinal investigation. *J. Child Psychol. Psychiatry* **65**, 1037–1046 (2024).

42. Smith, J. et al. Regulation of stress-induced sleep fragmentation by preoptic glutamatergic neurons. *Curr. Biol.* **34**, 12–23.e5 (2024).

43. Ye, L. et al. Ethanol abolishes vigilance-dependent astroglia network activation in mice by inhibiting norepinephrine release. *Nat. Commun.* **11**, 1–20 (2020).

44. Ren, S. et al. A midbrain GABAergic circuit constrains wakefulness in a mouse model of stress. *Nat. Commun.* **15**, 1–17 (2024).

45. Bartlang, M. S., Oster, H. & Helfrich-Förster, C. Repeated psychosocial stress at night affects the circadian activity rhythm of male mice. *J. Biol. Rhythms* **30**, 228–241 (2015).

46. Liu, M. Y. et al. Sucrose preference test for measurement of stress-induced anhedonia in mice. *Nat. Protoc.* **13**, 1686–1698 (2018).

47. Dieterich, A., Liu, T. & Samuels, B. A. Chronic non-discriminatory social defeat stress reduces effort-related motivated behaviors in male and female mice. *Transl. Psychiatry* **11**, 1–12 (2021).

48. Kotz, C. M. Integration of feeding and spontaneous physical activity: role for orexin. *Physiol. Behav.* **88**, 294–301 (2006).

49. Burdakov, D. Reactive and predictive homeostasis: Roles of orexin/hypocretin neurons. *Neuropharmacology* **154**, 61–67 (2019).

50. Dawson, M., Terstege, D. J., Epp, J. R., Leininger, G. M. & Sargin Correspondence, D. Hypocretin/orexin neurons encode social discrimination and exhibit a sex-dependent necessity for social interaction. *Cell Rep.* **42** (2023).

51. Sakurai, T. The role of orexin in motivated behaviours. *Nat. Rev. Neurosci.* **15**, 719–731 (2014).

52. Burt, J., Alberto, C. O., Parsons, M. P. & Hirasawa, M. Local network regulation of orexin neurons in the lateral hypothalamus. *Am. J. Physiol. Regul. Integr. Comp. Physiol.* **301**, 572–580 (2011).

53. Wollmann, G., Acuna-Goycolea, C. & Van Den Pol, A. N. Direct excitation of hypocretin/orexin cells by extracellular ATP at P2X receptors. *J. Neurophysiol.* **94**, 2195–2206 (2005).

54. Huang, H. et al. Cannabinoids excite hypothalamic melanin-concentrating hormone but inhibit hypocretin/orexin neurons: implications for cannabinoid actions on food intake and cognitive arousal. *J. Neurosci.* **27**, 4870–4881 (2007).

55. Clasadonte, J., Scemes, E., Wang, Z., Boison, D. & Haydon, P. G. Connexin 43-mediated astroglial metabolic networks contribute to the regulation of the sleep-wake cycle. *Neuron* **95**, 1365–1380.e5 (2017).

56. Braga, A., Chiacchiaretta, M., Pellerin, L., Kong, D. & Haydon, P. G. Astrocytic metabolic control of orexinergic activity in the lateral hypothalamus regulates sleep and wake architecture. *Nat. Commun.* **15**, 1–15 (2024).

57. Peña, C. J. et al. Early life stress alters transcriptomic patterning across reward circuitry in male and female mice. *Nat. Commun.* **10** (2019).

58. Depaauw-Holt, L., Peyrard, S., Bosson, A. & Murphy-Royal, C. Development and validation of stress paradigms to study astrocytes in rodent models of stress disorders. *Methods Mol. Biol.* **2896**, 215–222 (2025).

59. Lightman, S. L., Birnie, M. T. & Conway-Campbell, B. L. Dynamics of ACTH and cortisol secretion and implications for disease. *Endocr. Rev.* **41**, 470–490 (2020).

60. Huang, G. et al. Circadian misalignment leads to changes in cortisol rhythms, blood biochemical variables and serum miRNA profiles. *Biochem. Biophys. Res. Commun.* **567**, 9–16 (2021).

61. Min, L. Functional hypercortisolism, visceral obesity and metabolic syndrome. *Endocr. Pr.* **22**, 506 (2016).

62. Hasenmajer, V. et al. The immune system in Cushing's syndrome. *Trends Endocrinol. Metab.* **31**, 655–669 (2020).

63. O'Byrne, N. A., Yuen, F., Butt, W. Z. & Liu, P. Y. Sleep and circadian regulation of cortisol: a short review. *Curr. Opin. Endocr. Metab. Res.* **18**, 178–186 (2021).

64. Rodenbeck, A., Huether, G., Rüther, E. & Hajak, G. Interactions between evening and nocturnal cortisol secretion and sleep parameters in patients with severe chronic primary insomnia. *Neurosci. Lett.* **324**, 159–163 (2002).

65. Cui, X. Y. et al. Sleep patterns deteriorate over time in chronic corticosterone-treated rats. *Neurosci. Lett.* **682**, 74–78 (2018).

66. DeVallance, E. et al. Effect of chronic stress on running wheel activity in mice. *PLoS ONE* **12**, e0184829 (2017).

67. Singleton, J. M. & Garland, T. Jr. Influence of corticosterone on growth, home-cage activity, wheel running, and aerobic capacity in house mice selectively bred for high voluntary wheel-running behavior. *Physiol. Behav.* **198**, 27–41 (2019).

68. Bale, T. L. & Epperson, C. N. Sex differences and stress across the lifespan. *Nat. Neurosci.* **18**, 1413–1420 (2015).

69. Walker, D. M. et al. Sex-specific transcriptional changes in response to adolescent social stress in the brain's reward circuitry. *Biol. Psychiatry* **91**, 118–128 (2022).

70. Schuler, H. et al. Data-driven analysis identifies female-specific social modulation deficit after chronic social defeat stress. *bioRxiv* <https://doi.org/10.1101/2024.05.08.593167> (2024).

71. Geiger, L. T. et al. Early-life stress alters chromatin modifications in VTA to prime stress sensitivity. *bioRxiv* <https://doi.org/10.1101/2024.03.14.584631> (2024).

72. Peña, C. J. et al. Early life stress confers lifelong stress susceptibility in mice via ventral tegmental area OTX2. *Science* **356**, 1185–1188 (2017).

73. Wuertz-Kozak, K. et al. Effects of early life stress on bone homeostasis in mice and humans. *Int. J. Mol. Sci.* **21**, 1–25 (2020).

74. Söderholm, J. D. et al. Neonatal maternal separation predisposes adult rats to colonic barrier dysfunction in response to mild stress. *Am. J. Physiol. Gastrointest. Liver Physiol.* **283**, 1257–1263 (2002).

75. Rhodes, J. S., Gammie, S. C. & Garland, T. Neurobiology of mice selected for high voluntary wheel-running activity. *Integr. Comp. Biol.* **45**, 438–455 (2005).

76. Ruegsegger, G. N., Brown, J. D., Kovarik, M. C., Miller, D. K. & Booth, F. W. Mu-opioid receptor inhibition decreases voluntary wheel running in a dopamine-dependent manner in rats bred for high voluntary running. *Neuroscience* **339**, 525–537 (2016).

77. Fuss, J. et al. Hippocampal serotonin-1A receptor function in a mouse model of anxiety induced by long-term voluntary wheel running. *Synapse* **67**, 648–655 (2013).

78. Tesmer, A. L. et al. Orexin neurons mediate temptation-resistant voluntary exercise. *Nature Neuroscience* 1–9. <https://doi.org/10.1038/s41593-024-01696-2> (2024).

79. Kotz, C. M., Teske, J. A., Levine, J. A. & Wang, C. F. Feeding and activity induced by orexin A in the lateral hypothalamus in rats. *Regul. Pept.* **104**, 27–32 (2002).

80. Belle, M. D. C. & Piggins, H. D. Circadian regulation of mouse suprachiasmatic nuclei neuronal states shapes responses to orexin. *Eur. J. Neurosci.* **45**, 723–732 (2017).

81. Viskaitis, P. et al. Orexin neurons track temporal features of blood glucose in behaving mice. *Nat. Neurosci.* **27**, 1299–1308 (2024).

82. Karnani, M. M. et al. Activation of central orexin/hypocretin neurons by dietary amino acids. *Neuron* **72**, 616–629 (2011).

83. Williams, R. H., Alexopoulos, H., Jensen, L. T., Fugger, L. & Burdakov, D. Adaptive sugar sensors in hypothalamic feeding circuits. *Proc. Natl. Acad. Sci. USA* **105**, 11975–11980 (2008).

84. Agostinelli, L. J. et al. Descending projections from the basal forebrain to the orexin neurons in mice. *J. Comp. Neurol.* **525**, 1668–1684 (2017).

85. Ferrari, L. L. et al. Regulation of Lateral Hypothalamic Orexin Activity by Local GABAergic Neurons. *J. Neurosci.* **38**, 1588–1599 (2018).

86. Burdakov, D., Gerasimenko, O. & Verkhratsky, A. Physiological changes in glucose differentially modulate the excitability of hypothalamic melanin-concentrating hormone and orexin neurons *in situ*. *J. Neurosci.* **25**, 2429–2433 (2005).

87. Eggermann, E. et al. The wake-promoting hypocretin-orexin neurons are in an intrinsic state of membrane depolarization. *J. Neurosci.* **23**, 1557–1562 (2003).

88. Grafe, L. A., Cornfeld, A., Luz, S., Valentino, R. & Bhatnagar, S. Orexins mediate sex differences in the stress response and in cognitive flexibility. *Biol. Psychiatry* **81**, 683 (2017).

89. Wei, F. et al. Chronic stress impairs the aquaporin-4-mediated glymphatic transport through glucocorticoid signaling. *Psychopharmacology (Berl.)* **236**, 1367–1384 (2019).

90. Murphy-Royal, C., Gordon, G. R. & Bains, J. S. Stress-induced structural and functional modifications of astrocytes—Further implicating glia in the central response to stress. *Glia* **67**, 1806–1820 (2019).

91. Di Benedetto, B. et al. Fluoxetine requires the endfeet protein aquaporin-4 to enhance plasticity of astrocyte processes. *Front Cell Neurosci.* **10**, 174937 (2016).

92. Fan, J. et al. O-GlcNAc transferase in astrocytes modulates depression-related stress susceptibility through glutamatergic synaptic transmission. *J. Clin. Invest.* **133** (2023).

93. Bollinger, J. L., Johnsmael, S., Vollmer, L. L., Kuhn, A. M. & Wohleb, E. S. Stress-induced dysfunction of neurovascular astrocytes contributes to sex-specific behavioral deficits. *bioRxiv* <https://doi.org/10.1101/2024.05.14.594147> (2024).

94. Depaauw-Holt, L., Peyrard, S., Bosson, A. & Murphy-Royal, C. Morphological Investigation of astrocytic responses to stress. *Methods Mol. Biol.* **2896**, 231–241 (2025).

95. Adamantidis, A. R., Zhang, F., Aravanis, A. M., Deisseroth, K. & De Lecea, L. Neural substrates of awakening probed with optogenetic control of hypocretin neurons. *Nature* **450**, 420–424 (2007).

96. Tsunematsu, T. et al. Acute optogenetic silencing of orexin/hypocretin neurons induces slow-wave sleep in mice. *J. Neurosci.* **31**, 10529–10539 (2011).

97. Nagai, J. et al. Specific and behaviorally consequential astrocyte Gq GPCR signaling attenuation in vivo with iβARK. *Neuron* **109**, 2256–2274.e9 (2021).

98. Yu, X. et al. Reducing astrocyte calcium signaling in vivo alters striatal microcircuits and causes repetitive behavior. *Neuron* **99**, 1170–1187.e9 (2018).

99. Srinivasan, R. et al. Ca²⁺ signaling in astrocytes from *Ip3r2* *−/−* mice in brain slices and during startle responses in vivo. *Nat. Neurosci.* **18**, 708–717 (2015).

100. Farhy-Tselnicker, I. et al. Activity-dependent modulation of synapse-regulating genes in astrocytes. *Elife* **10** (2021).

101. Panatier, A. et al. Astrocytes are endogenous regulators of basal transmission at central synapses. *Cell* **146**, 785–798 (2011).

102. Vaidyanathan, T. V., Collard, M., Yokoyama, S., Reitman, M. E. & Poskanzer, K. E. Cortical astrocytes independently regulate sleep depth and duration via separate gpcr pathways. *Elife* **10**, (2021).

103. Pascual, O. et al. Neurobiology: Astrocytic purinergic signaling coordinates synaptic networks. *Science* **310**, 113–116 (2005).

104. Zhang, J. M. et al. ATP released by astrocytes mediates glutamatergic activity-dependent heterosynaptic suppression. *Neuron* **40**, 971–982 (2003).

105. Carlsén, E. M. & Perrier, J. F. Purines released from astrocytes inhibit excitatory synaptic transmission in the ventral horn of the spinal cord. *Front Neural Circuits* **8**, 60 (2014).

106. Li, H. et al. Astrocytes release ATP/ADP and glutamate in flashes via vesicular exocytosis. *Mol. Psychiatry* 1–15 <https://doi.org/10.1038/s41380-024-02851-8> (2024).

107. Koyanagi, S. et al. Glucocorticoid regulation of ATP release from spinal astrocytes underlies diurnal exacerbation of neuropathic mechanical allodynia. *Nat. Commun.* **7**, 1–13 (2016).

108. Lefton, K. B. et al. Norepinephrine signals through astrocytes to modulate synapses. *Science* **388**, 776–783 (2025).

109. Gordon, G. R. J. et al. Astrocyte-mediated distributed plasticity at hypothalamic glutamate synapses. *Neuron* **64**, 391–403 (2009).

110. Florenzano, F. et al. P2X2R purinergic receptor subunit mRNA and protein are expressed by all hypothalamic hypocretin/orexin neurons. *J. Comp. Neurol.* **498**, 58–67 (2006).

111. Hario, S. et al. High-performance genetically encoded green fluorescent biosensors for intracellular L-lactate. *ACS Cent. Sci.* **10**, 402–416 (2024).

112. Du, J. et al. S100B is selectively expressed by gray matter protoplasmic astrocytes and myelinating oligodendrocytes in the developing CNS. *Mol. Brain* **14**, 1–11 (2021).

113. Deloulme, J. C. et al. Nuclear expression of S100B in oligodendrocyte progenitor cells correlates with differentiation toward the oligodendroglial lineage and modulates oligodendrocytes maturation. *Mol. Cell Neurosci.* **27**, 453–465 (2004).

114. Torres-Berrio, A., Bortolami, A., Peña, C. J. & Eric, J. N. Neurobiology of resilience to early life stress. *Neuropsychopharmacol* <https://doi.org/10.1038/s41386-025-02158-4> (2025).

115. Ventriglio, A., Gentile, A., Baldessarini, R. J. & Bellomo, A. Early-life stress and psychiatric disorders: epidemiology, neurobiology and innovative pharmacological targets. *Curr. Pharm. Des.* **21**, 1379–87 (2015).

116. Zhang, Y. et al. An RNA-sequencing transcriptome and splicing database of glia, neurons, and vascular cells of the cerebral cortex. *J. Neurosci.* **34**, 11929–11947 (2014).

117. Davis, A. B., Lloyd, K. R., Bollinger, J. L., Wohleb, E. S. & Reyes, T. M. Adolescent high fat diet alters the transcriptional response of microglia in the prefrontal cortex in response to stressors in both male and female mice. *Stress* **27** (2024).

118. Woodburn, S. C. et al. Depletion of microglial BDNF increases susceptibility to the behavioral and synaptic effects of chronic unpredictable stress. *Brain Behav. Immun.* **109**, 127–138 (2023).

119. Hösl, L. et al. Direct vascular contact is a hallmark of cerebral astrocytes. *Cell Rep.* **39**, 110599 (2022).

120. Tran, C. H. T., Peringod, G. & Gordon, G. R. Astrocytes integrate behavioral state and vascular signals during functional hyperemia. *Neuron* **100**, 1133–1148.e3 (2018).

121. González-Vila, A. et al. Astrocytic insulin receptor controls circadian behavior via dopamine signaling in a sexually dimorphic manner. *Nat. Commun.* **14**, 1–21 (2023).

122. Fernandez, A. M. et al. Insulin regulates neurovascular coupling through astrocytes. <https://doi.org/10.1073/pnas> (2022).

123. García-Cáceres, C. et al. Astrocytic insulin signaling couples brain glucose uptake with nutrient availability. *Cell* **166**, 867–880 (2016).

124. Kim, J. G. et al. Leptin signaling in astrocytes regulates hypothalamic neuronal circuits and feeding. *Nat. Neurosci.* **17**, 908–910 (2014).

125. Fuente-Martín, E. et al. Ghrelin regulates glucose and glutamate transporters in hypothalamic astrocytes. *Sci. Rep.* **6**, 1–15 (2016).

126. Murphy-Royal, C., Ching, S. N. & Papouin, T. A conceptual framework for astrocyte function. *Nat. Neurosci.* **26**, 1848–1856 (2023).

127. Bouyakdan, K. et al. The gliotransmitter ACBP controls feeding and energy homeostasis via the melanocortin system. *J. Clin. Invest.* **129**, 2417–2430 (2019).

Acknowledgements

The authors thank Aurélie Cleret-Buhot (CRCHUM cellular imaging core) for microscopy training and the staff of the animal facility at the CRCHUM. Fonds de Recherche du Québec—Santé (FRQS; 296562 and 309889), CHUM Foundation, Fondation Courtois grant, the Scottish Rite Charitable Foundation of Canada (24109), CIHR project grant (478629) and Natural Science and Engineering Council of Canada Discovery Grant (RGPIN-2021-03211) to C.M.-R., and the Réseau Québécois sur le Suicide les troubles de l'humeur et les troubles Associées (RQSHA) pilot grant to L.R.D.-H. and C.M.-R. L.R.D.-H. was supported by a FRQS doctoral award. B.R. was supported by a Canada Graduate Scholarship Master's award and a recruitment award from Neuroscience Dept. Université de Montréal. C.M.-R. was supported by Junior 1 and Junior 2 Chercheur-Boursier salary awards from FRQS.

Author contributions

L.R.D.-H. and C.M.-R. designed the study. L.R.D.-H. carried out behavioural experiments, immunostaining and analysis of subsequent data. L.R.D.-H. and S.H. carried out morphological analysis. L.R.D.-H. took

blood samples and performed ELISA experiments. M.D. carried out metabolic phenotyping under supervision of T.A. and C.M.-R. L.R.D.-H. and A.B. carried out injection of viral vectors. L.R.D.-H. and B.R. carried out electrophysiological experiments. L.R.D.-H. carried out validation of viral expression. C.I. carried out immunostaining and analysis for synaptic counts. L.R.D.-H. carried out pharmacology experiments and two-photon imaging. L.R.D.-H. carried out analysis of subsequent data. Y.N. developed and provided fluorescent sensors for L-lactate. S.P. maintained and generated mouse colonies. S.F. provided expertise regarding running wheel experiment and analysis. L.R.D.-H. and C.M.-R. wrote the manuscript. All authors approved the final version of the manuscript.

Competing interests

The authors declare no competing interests.

Additional information

Supplementary information The online version contains supplementary material available at <https://doi.org/10.1038/s41467-025-61643-y>.

Correspondence and requests for materials should be addressed to Ciaran Murphy-Royal.

Peer review information *Nature Communications* thanks Olga Barca-Mayo, Catherine Peña and Jun Nagai for their contribution to the peer review of this work. A peer review file is available.

Reprints and permissions information is available at <http://www.nature.com/reprints>

Publisher's note Springer Nature remains neutral with regard to jurisdictional claims in published maps and institutional affiliations.

Open Access This article is licensed under a Creative Commons Attribution-NonCommercial-NoDerivatives 4.0 International License, which permits any non-commercial use, sharing, distribution and reproduction in any medium or format, as long as you give appropriate credit to the original author(s) and the source, provide a link to the Creative Commons licence, and indicate if you modified the licensed material. You do not have permission under this licence to share adapted material derived from this article or parts of it. The images or other third party material in this article are included in the article's Creative Commons licence, unless indicated otherwise in a credit line to the material. If material is not included in the article's Creative Commons licence and your intended use is not permitted by statutory regulation or exceeds the permitted use, you will need to obtain permission directly from the copyright holder. To view a copy of this licence, visit <http://creativecommons.org/licenses/by-nc-nd/4.0/>.

© The Author(s) 2025